

Numerical solution of the 2+1 Teukolsky equation on a hyperboloidal and horizon penetrating foliation of Kerr and application to late-time decays

Enno Harms, Sebastiano Bernuzzi, and Bernd Brügmann

Theoretical Physics Institute, University of Jena, 07743 Jena, Germany

Abstract. In this work we present a formulation of the Teukolsky equation for generic spin perturbations on the hyperboloidal and horizon penetrating foliation of Kerr recently proposed by Rácz and Tóth. An additional, spin-dependent rescaling of the field variable can be used to achieve stable, long-term, and accurate time-domain evolutions of generic spin perturbations. As an application (and a severe numerical test), we investigate the late-time decays of electromagnetic and gravitational perturbations at the horizon and future null infinity by means of 2+1 evolutions. As initial data we consider four combinations of (non-)stationary and (non-)compact-support initial data with a pure spin-weighted spherical harmonic profile. We present an extensive study of late time decays of axisymmetric perturbations. We verify the power-law decay rates predicted analytically, together with a certain “splitting” behaviour of the power-law exponent. We also present results for non-axisymmetric perturbations. In particular, our approach allows to study the behaviour of the late time decays of gravitational fields for nearly extremal and extremal black holes. For rapid rotation we observe a very prolonged, weakly damped, quasi-normal-mode phase. For extremal rotation the field at future null infinity shows an oscillatory behaviour decaying as the inverse power of time, while at the horizon it is amplified by several orders of magnitude over long timescales. This behaviour can be understood in terms of the superradiance cavity argument.

1. Introduction

The Teukolsky equation (TE) [1, 2] describes linear perturbations of a field Ψ of spin s around the Kerr black hole solution. Black hole perturbation theory [3] has widespread applications in general/mathematical relativity and, ultimately, in astrophysics. To give a few examples, the study of TE solutions is related to fundamental topics like the stability of Kerr [4, 5, 6, 7], no-hair theorems [8, 9, 10], black hole quasi-normal-modes (QNMs) [11], and gravitational radiation from binary systems within the post-Newtonian approximation [12], the test-mass [13, 14, 15, 16], or the self-force (see e.g. [17] for a recent work and [18] for a review) approximations.

The TE is separable if a Fourier transform in time is performed simultaneously with the one in the angular azimuthal direction (axisymmetric background). Exploiting this fact, most of the numerical calculations have been performed in the frequency domain. Time-domain numerical solutions of the TE are mainly limited to the scalar case ($s = 0$), which is extensively investigated also in multidimensional simulations, see e.g. [19, 20, 21, 22, 23, 24, 25]. The relevant case of gravitational perturbations ($s = -2$) has been considered for the first time by Krivan et al. [26]. There, compact-support initial data have been evolved with the 2+1 mode-decomposed homogeneous TE using a particular first order reduction and a Lax-Wendroff second order scheme. The same approach has been extended to fourth order accuracy in the radial direction in [27], and considered in comparison to an approximate 1+1 approach in [28]. To date, the numerical scheme of [26] is, to our knowledge, the only successful method to solve the TE in the time domain for a generic spin field, and it has been applied in late-time decay studies of gravitational perturbations (at finite radius) [26, 29, 27], and in simulations of gravitational waves from a particle plunging into a rotating black hole [30, 31, 32, 33].

A long-standing problem in perturbation theory of black holes is the study of the late-time decay of the perturbative field, the so-called “tail”. Pioneering work by Price [34] pointed out that the scattering of a scalar field off a non-rotating black hole is characterized by a power-law late-time decay $\propto t^{-\mu}$, the decay rate μ depending on the particular multipoles of the radiation considered and on the initial data employed. The behaviour can be related to the asymptotic form (large radii) of the black hole potential. Similar considerations hold for the gravitational case described by the Regge-Wheeler-Zerilli equations [35, 36] which have been studied in several works, e.g. [37, 38, 39, 40, 41, 42]. Working in null-cone coordinates, Gundlach et al. [43] have computed for the first time the decay rates at future null infinity (\mathcal{I}^+) of scalar and electromagnetic perturbations of non-rotating black holes. It was found that they are different from those at finite radii.

The numerical work of Krivan et al. [19, 26] considered for the first time the problem of late-time decay of fields on Kerr. As expected, the rotation of the background causes mode coupling (or mode mixing) between the polar modes, labelled by the integer l . In this paper we will often refer to the projections of a field against these polar modes as the

smoothly connects the horizon with future null-infinity. References [24, 25] pointed out an intermediate “splitting” behaviour of the decay rates of scalar fields on Kerr at finite radius. The phenomenon was clarified in [61] using a horizon penetrating, hyperboloidal foliation constructed with transmitting layers (see [62] and references therein).

Finally, Andersson and Glampedakis [63, 29] have shown that the late time decay of non-axisymmetric perturbations of rapidly spinning black holes is not characterized by a Price-like power law but dominated by the QNM contribution. In particular, for nearly extremal black holes, the collective effect from several, slowly damped QNMs results in an oscillatory and weakly exponentially damped signal. In contrast, for extremal black holes the weakly damped QNMs combine to give asymptotically an overall decay rate $\propto t^{-1}$.

In this paper we consider a novel formulation of the TE on the hyperboloidal and horizon-penetrating foliation of RT, and perform numerical experiments in the time domain studying the late time decay of generic spin perturbations of Kerr. The use of hyperboloidal and horizon penetrating foliations with compactification of null infinity has two well-known properties, e.g. [64, 65]: (i) \mathcal{I}^+ and the horizon are included in the computational domain, thus allowing an unambiguous extraction of the radiation, (ii) artificial boundary conditions are not needed for the solution of the Cauchy problem. The late time decay problem is a severe test for the robustness and accuracy of a numerical scheme for the TE. Note also that, for instance, Price-like power law tails can not arise if Sommerfeld-type artificial boundary conditions are employed [66]. Here, we compute numerically, for the first time to our knowledge, late-time decay rates for gravitational and electromagnetic perturbations of Kerr both at the horizon and at future null infinity.

The paper is organized as follows. In Sec. 2 the novel formulation of the TE on the RT foliation is described. The key addition to the construction of RT is a s -dependent rescaling of the master variable, resulting in equation coefficients regular over the whole domain of integration. A two-parameter family of (RT-like) coordinate transformations is also given. In Sec. 3 the numerical method employed is detailed. In Sec. 4 we give an overview of the numerical experiments performed, including convergence tests and a discussion of numerical difficulties. In Sec. 5 results for power law decay rates are presented in the axisymmetric case ($m = 0$). In Sec. 6 results for late time decays for a few non-axisymmetric cases are presented ($s = 0, -2$). We conclude in Sec. 7. In Appendix A the TE coefficients are stated in RT coordinates. In Appendix B the analytic calculation of the Green’s function of [46] is reviewed.

Geometric units ($c = G = 1$) are employed.

2. Teukolsky equation on the RT foliation

In this section we review the construction of the RT coordinates, present a two-parameter generalization and derive a form of the TE with coefficients regular at \mathcal{I}^+ and the horizon for every spin field value s . In the scalar case, $s = 0$, the equation reduces to

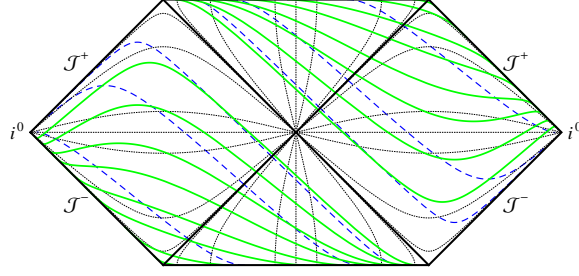


Figure 1. Conformal diagram for the Schwarzschild spacetime ($a = 0$). The τ -slices (Kerr ingoing coordinates) are the dashed blue lines, the T -slices (RT coordinates) are the solid green lines, the t -slices (BL coordinates) are the dotted black lines.

the one given in RT, modulo an overall factor.

2.1. The RT foliation

Rácz and Tóth [24] have proposed a hyperboloidal foliation of Kerr that penetrates the horizon and reaches future null infinity. The foliation can be explicitly constructed from the Kerr solution in Boyer-Lindquist (BL) coordinates $x^\mu = \{t, r, \theta, \phi\}$ by two successive coordinate transformations. To fix the notation, we recall the Kerr metric in BL coordinates

$$g_{\text{BL}} = - \left(1 - \frac{2Mr}{\rho} \right) dt^2 - \frac{4aMr}{\rho} \sin^2 \theta dt d\varphi + \frac{\rho}{\Delta} dr^2 + \rho d\theta^2 + \left(r^2 + a^2 + \frac{2Ma^2r \sin^2 \theta}{\rho} \right) \sin^2 \theta d\varphi^2, \quad (2)$$

where M and aM are the mass and angular momentum of the black hole, $\rho = r^2 + a^2 \cos^2 \theta$, and $\Delta = r^2 - 2Mr + a^2 := (r - r_+)(r - r_-)$. The two step procedure to construct the RT foliation is the following. First, switch to ingoing-Kerr coordinates $x^\mu = \{\tau, r, \theta, \varphi\}$ defined by

$$\tau = t - r + \int dr \frac{a^2 + r^2}{\Delta} \quad (3)$$

$$\varphi = \phi + a \int \frac{dr}{\Delta}. \quad (4)$$

Second, introduce the coordinates $x^a = \{T, R, \theta, \varphi\}$ such that

$$\tau = T - 4M \log(|1 - R^2|) + \frac{1 + R^2}{1 - R^2} \quad (5)$$

$$r = \frac{2R}{1 - R^2}. \quad (6)$$

The transformation in Eq. (5)-(6) realizes a hyperboloidal and horizon penetrating foliation with \mathcal{I}^+ compactified at $R = 1$ [58, 59] and the r_+ horizon located at

$$R_+ = \frac{2\sqrt{2M\sqrt{M^2 - a^2} - a^2 + 2M^2 + 1} - 2}{2(\sqrt{M^2 - a^2} + M)}. \quad (7)$$

Note that R_+ depends on M and a . In Fig. 1 (compare Fig. 1 of RT) the two foliations of the spacetime are shown in the non-rotating $a = 0$ limit for simplicity.

Following [58, 59, 24] we can also write Eq. (5)-(6) in the more general form

$$\tau = T + \sqrt{\kappa^2 + (R/\Omega(R))^2} - 4M \log(2\Omega(R)) \quad (8)$$

$$r = \frac{R}{\Omega_S(R)}, \quad (9)$$

where $\Omega_S(R)$ is a general *compress function* [65] (eventually containing a parameter S to fix the coordinate location of \mathcal{I}^+) and κ is a parameter determining the coordinate speed of the outgoing characteristic at null infinity (in RT $\kappa = S = 1$).

2.2. Scaling the TE master variable

The homogeneous TE in BL coordinates reads

$$\begin{aligned} D^2 \partial_{tt} \Psi &= -\Delta^{-1} 4aMr \partial_{\varphi t} \Psi + \Delta^{-s} \partial_r (\Delta^{s+1} \partial_r \Psi) + \sin \theta^{-1} \partial_\theta (\sin \theta \partial_\theta \Psi) \\ &+ (\sin \theta^{-2} - a^2 \Delta^{-1}) \partial_{\varphi\varphi} \Psi - 2s(\Delta^{-1} M(a^2 - r^2) + (r + ia \cos \theta)) \partial_t \Psi \\ &+ 2s(\Delta^{-1} a(r - M) + i \cot \theta \sin \theta^{-1}) \partial_\varphi \Psi - s(s \cot \theta^2 - 1) \Psi, \end{aligned} \quad (10)$$

where $D^2 = (r^2 + a^2)\Delta^{-1} - a^2 \sin^2 \theta$. The introduction of a conformal compactification like that of Eqs (8)-(9) requires to rescale the field variable like

$$\Psi = r^{-(2s+1)} \psi, \quad (11)$$

in order to avoid the singularity of the physical metric at \mathcal{I}^+ that is induced also in the wave equation [64, 24]. However, once Eq. (10) is expressed in RT coordinates that include the horizon, some coefficients have singularities on the horizon if $s \neq 0$. The simple rescaling

$$\Psi = r^{-(2s+1)} (\Delta r^{-2})^{-s} \psi = \Delta^{-s} r^{-1} \psi, \quad (12)$$

or

$$\Psi = \Delta(R)^{-s} \frac{R}{\Omega(R)} \psi, \quad (13)$$

cures the singularities. Note that the factor $1/r^2$ in the term $(\Delta r^{-2})^{-s}$ is essential since $\Delta \sim r^2$ for $r \rightarrow \infty$. The rescaling in Eq. (12) has been, in some form, widely used in the literature about the TE since [2], and thus should be considered as the “natural” one. In connection with the hyperboloidal transformation, it has been recently considered in the frequency domain framework of [67] (see Eq. (13) there). For time-domain studies

it is employed here for the first time together with the RT coordinates (Eq. 13). The resulting TE is of the form

$$\begin{aligned} C_0\psi + C_T\partial_T\psi + C_R\partial_R\psi + C_\theta\partial_\theta\psi + C_\varphi\partial_\varphi\psi + C_{TT}\partial_{TT}\psi + C_{RR}\partial_{RR}\psi \\ + C_{\theta\theta}\partial_{\theta\theta}\psi + C_{\varphi\varphi}\partial_{\varphi\varphi}\psi + C_{R\varphi}\partial_{R\varphi}\psi + C_{TR}\partial_{TR}\psi + C_{T\varphi}\partial_{T\varphi}\psi = 0 \end{aligned} \quad , \quad (14)$$

where the coefficients are given explicitly in Appendix A. As one can check from direct inspection, the coefficients are rational polynomials and they are regular over the domain $R \in [R_+, 1]$. This property holds also for the general rescaling in Eqs. (8)-(9). Note that the new variable ψ is asymptotically constant, for example for $s = -2$ it is related to the Weyl scalar Ψ_4 by $\psi = r \Psi_4$, since $\Psi \sim r^4 \Psi_4$ asymptotically. Note also that the equation in the time domain is not separable in the standard way due to the term $\propto \partial_{\varphi t}$.

For numerical applications Eq. (14) can be decomposed in 2+1 form separating each Fourier m -mode in the azimuthal direction and exploiting the axisymmetry of the background. The resulting 2+1 equation has the form

$$\tilde{C}_0\psi + \tilde{C}_T\partial_T\psi + \tilde{C}_\theta\partial_\theta\psi + \tilde{C}_R\partial_R\psi + \tilde{C}_{TT}\partial_{TT}\psi + \tilde{C}_{RR}\partial_{RR}\psi + \tilde{C}_{\theta\theta}\partial_{\theta\theta}\psi + \tilde{C}_{TR}\partial_{TR}\psi = 0 \quad , \quad (15)$$

with coefficients presented in Appendix A, and the index m in the field variable ψ_m has been suppressed for brevity.

2.3. The initial-boundary value problem

From a PDE point of view, Eq. (14) (as Eq. (10)) is a 3+1 linear wave equation with variable coefficients in spherical coordinates. The principal part of the equation is independent of the spin weight, hence symmetric hyperbolicity and well-posedness of the Cauchy problem follow from the scalar $s = 0$ case when appropriate boundaries are considered \ddagger .

An advantage of using a hyperboloidal foliation and compactification is that no artificial timelike outer boundary condition is needed, e.g. [65]. Furthermore, because the foliation is horizon penetrating, also the inner boundary condition is not needed. Inspection of the equation at $R = 1$ and $R = R_+$ gives that both boundaries are “outflow” boundaries. Taking the limits $R \rightarrow R_+$ and $R \rightarrow 1$ of Eq. (14) with $M = 1$ (and omitting the angular terms and the non-principal part for simplicity) one obtains

$$\partial_T \left(\tilde{C}_{TT}\partial_T\psi + \tilde{C}_{TR}\partial_R\psi \right) = 0 \quad . \quad (16)$$

The speeds, $c_R(R, \theta) = \tilde{C}_{TR}/\tilde{C}_{TT}$, for $a = 0$ are given by

$$\begin{aligned} c_{R,-}(R_+, \frac{\pi}{2}) &\simeq -0.0460655 \quad , \\ c_{R,+}(1, \frac{\pi}{2}) &= 0.08 \quad . \end{aligned} \quad (17)$$

\ddagger Numerical instabilities can still arise from unstable discretization, stiff non-principal terms, or exponentially growing continuum modes triggered by numerical noise.

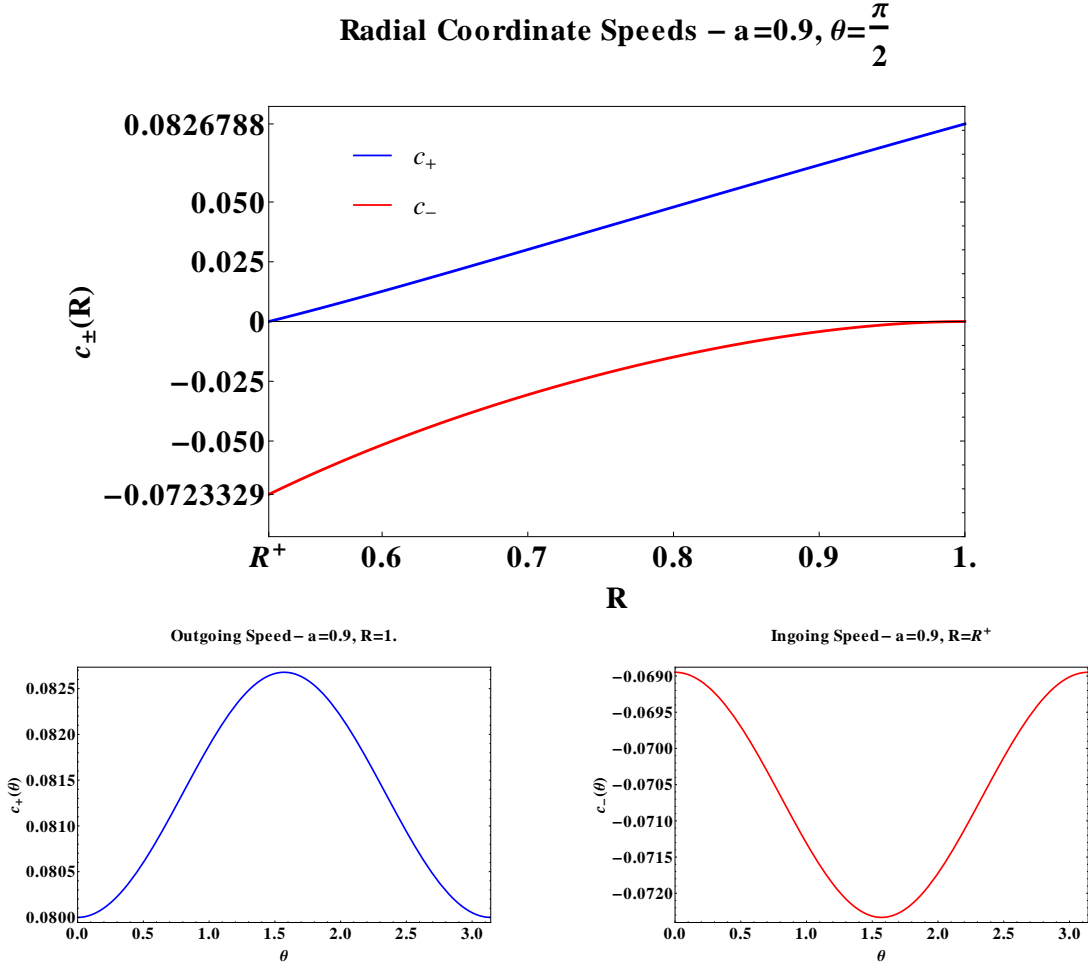


Figure 2. Radial coordinate speeds for $M = 1$ and $a = 0.9$. Different panels show the functional dependences on R and θ , $c_{\pm}(R, \theta)$. Because the incoming (outgoing) coordinate speed vanishes at the outer (inner) boundary artificial boundary conditions are not needed. Note the weak dependence on θ for $a = 0.9$.

Similarly, one obtains for $a = 0.9$

$$\begin{aligned} c_{R,-}(R_+, \frac{\pi}{2}) &\simeq -0.0723329, \\ c_{R,+}(1, \frac{\pi}{2}) &\simeq 0.0826788. \end{aligned} \tag{18}$$

The speeds $c_{R,\pm}$ are the coordinate speeds of light in radial direction that can be in general calculated as

$$c_{R,+} = -\beta^R + \sqrt{\gamma^{RR}}\alpha, \quad c_{R,-} = -\beta^R - \sqrt{\gamma^{RR}}\alpha, \tag{19}$$

where α is the lapse, β^R the radial component of the shift vector, and γ^{RR} the radial component of the spatial 3-metric in RT coordinates (see Appendix A.) The speeds are illustrated in Fig. 2 for $M = 1$ and $a = 0.9$, and agree with the above estimates from the limiting equation.

3. Numerical method

In this section we describe two different numerical strategies implemented for the solution of the 2+1 TE.

The numerical algorithms rely in both cases on a method-of-lines approach for the time integration. Equation (15) (or Eq. (14)) is written in a first-order-in-time form,

$$\frac{du}{dt} = R(u) , \quad (20)$$

and evolved as an ODE system. Above u is a certain vector of real functions and $R(\cdot)$ a discrete representation of the right-hand-side of the system. A standard fourth order Runge-Kutta integrator is employed. The time step is chosen according to a Courant-Friedrich-Lewy (CFL) condition of type $\Delta t = C_{\text{CFL}} \min(h_R, h_\theta)$, where h_x is the minimum grid spacing in direction x and the factor C_{CFL} accounts for the maximum speed of the system. The spatial discretization is performed in two different ways, and the specific form of the first-order-in-time systems also differs.

The *PS-Teukode* implements a fully first-order reduction of Eq. (15) with reduction variables $\P u = \{\psi, \partial_T \psi, \partial_R \psi, \partial_\theta \psi\}$ and pseudo-spectral (PS) representation of first derivatives. The radial direction is covered by a Gauss-Lobatto grid and Chebychev polynomials are employed for the PS derivatives. The angular direction $\theta \in (0, \pi)$ is represented on a staggered equidistant grid with *double covering* (i.e. the function is extended to $\theta \in (0, 2\pi)$) in order to employ the Fourier basis for the derivatives, e.g. [68]. Differently from [68], here we extend the function by imposing a given parity. Specifically, by inspection of spin-weighted spherical harmonics, we assume the field ψ has parity $\pi = (-1)^{m+s}$ across the axis. We experimentally found that this prescription is important for long-term stability. Note that this assumption is compatible with the use of pure multipole initial data in the 3+1 equation and with generic initial data in the 2+1 equation. The *PS-Teukode* additionally implements the following options: (i) finite differencing derivatives in the radial direction (as described below); (ii) the 3+1 Eq. (14) by using the Fourier basis also in the azimuthal direction; (iii) different floating-point arithmetics: double, long-double and quadruple. Although quadruple precision requires several changes in the code, and since it is not available in standard hardware leads to a slow-down by a factor of ~ 50 , it turned out to be essential for the investigation of $s = -2$ decay rates.

The *FD-Teukode* implements a second-order reduction in space of Eq. (15) with reduction variables $u = \{\psi, \partial_T \psi\}$, and finite difference (FD) representation of the derivatives up to sixth order accuracy. The stencils in the radial direction are centered in the bulk of the domain and lop-sided at the boundaries. The angular grid is staggered (the same as in the PS code) and ghosts points are employed to implement the boundary conditions on the axis. The ghosts points are filled according to the parity condition

\P The ψ variable is complex, the split into real and imaginary part is understood and omitted in the formulas for brevity.

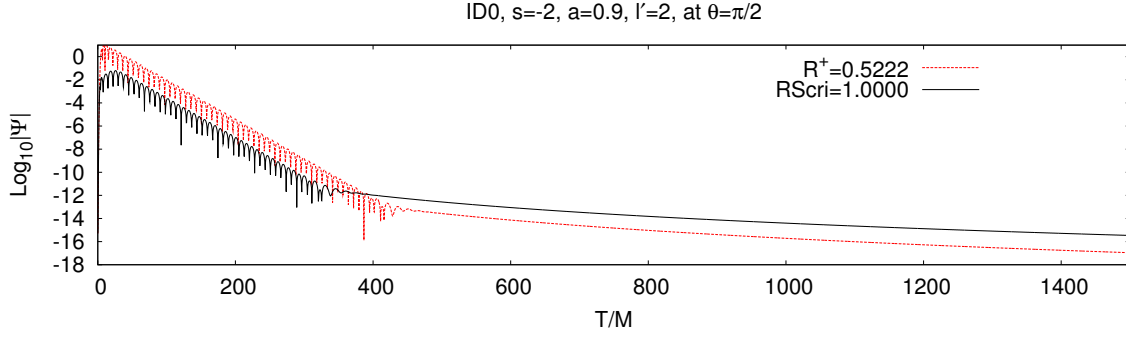


Figure 3. Evolution of the perturbation field at the horizon and \mathcal{S}^+ ($\theta = \pi/2$). The field is characterized by the quasi normal mode ringdown and a power law tail. The plot refers to a simulation of an axisymmetric gravitational perturbation ($s = -2$ and $m = 0$) with ID0, $l' = 2$ and $a = 0.9$.

$\pi = (-1)^{m+s}$. Artificial dissipation operators are also implemented and employed for long term stability.

Stable, long-term evolutions are obtained with both codes. In this paper we mainly restrict attention to the results obtained with the PS code (in some cases used with FD in the radial direction as indicated below) since the late time decays can be computed more accurately with this approach.

4. Overview of the numerical experiments

In this section the initial data employed, the code's convergence properties, and the methodology used in simulation data analysis are discussed. The black hole mass is set to $M = 1$ from now on in this paper, and the spin parameter is identified with the angular momentum, $a = J/M^2$.

Initial data are given specifying an angular profile, a radial profile, and the time derivative of the field. The angular profile is usually prescribed by a spin-weighted spherical harmonic multipole, i.e. $\psi(\theta) \propto {}^s Y_{l'm'}(\theta)$ (pure multipole initial data). Four initial data configurations are considered corresponding to different choices of radial profiles and the time derivative of the field. They are named ID0, ID1, ID2, and ID3, and defined by

$$\text{ID0 / ID2} : \begin{cases} \psi(0, R) &= G(R) / 1 \\ \partial_T \psi(0, R) &= 0 \end{cases} \quad (21)$$

$$\text{ID1 / ID3} : \begin{cases} \psi(0, R) &= 0 \\ \partial_T \psi(0, R) &= G(R) / 1, \end{cases} \quad (22)$$

with

$$G(R) = e^{-\frac{w}{2}(R-R_0)^2}. \quad (23)$$

These initial data are commonly used in the literature in which they are referred to as stationary (ID0, ID2) or non-stationary (ID1, ID3), and compact (ID0, ID1) or non-compact (ID2, ID3) support initial data. Note that, strictly speaking, a Gaussian is not of compact support but we verified that, with the parameters employed, the field value is below the round-off level at the horizon and \mathcal{I}^+ . For example setting $w = 3000$ and $R_0 = 0.8$, $G(R) \sim 10^{-38}$ at the horizon (for $a = 0.9$ $R_+ \approx 0.5222$) and at $R = 1$.

We performed evolutions with the different initial data and with different spin fields for black hole parameters $M = 1$ and $a = \{0, 0.5, 0.9\}$. The qualitative outcome of all the simulations is shown in Fig. 3 for the exemplary case $s = -2$, ID0 and $a = 0.9$. The figure displays the radiation field extracted at the horizon and at \mathcal{I}^+ for $\theta = \pi/2$. The solution has the well-known structure composed of an initial transient, the QNM phase, and the power law decay. We have checked frequencies and damping times of the QNMs in some cases

and found discrepancies below or of the order of 1% with the tables of Berti et al. [11]. For example, in the case of a $s = -2$ perturbation with $l' = 2$ on Schwarzschild ($a = 0$) the ringing frequency and the damping time are $(\omega, \tau) = (0.3876, 11.2361)$, to be compared with $(\omega, \tau) = (0.3737, 11.2410)$. For $l' = 3$ we find $(0.6133, 10.7958)$ in good agreement with $(0.5994, 10.7875)$. For $l' = 4$ we find $(0.8220, 10.6248)$ to be compared with $(0.8091, 10.6202)$, and similarly for other cases.

4.1. Convergence

Let us discuss the convergence tests performed to confirm the correct implementation of the code. The results confirm the expected exponential convergence of the PS code, as far as the solution does not develop high gradients and/or reaches amplitudes comparable to machine accuracy. At late times the radial profile of the solution develops strong gradients, essentially due to the different power indices μ at the horizon and \mathcal{I}^+ . The convergence rate is then slower, and progressively more coefficients are necessary to describe the solution. The particular shapes of these gradients depend also on s . Notably, in the cases $s > 0$, the computations are more efficiently performed with finite differencing in the radial direction.

Spectral convergence is monitored by looking at the expansion coefficients, c_k , of the spectral approximation. The highest accuracy achievable in the description of a *smooth* function is determined by round-off errors. Spectral convergence implies that the magnitudes of the coefficients c_k decay exponentially in k . We discuss here convergence of the PS code for a representative case, namely a $s = -2$, $a = 0.9$ simulation with ID0, $l' = 2$, and quadruple precision. We experimentally find that large CFL factors can be used without encountering stability problems, consistent with the small coordinate speeds of Eq.'s (17)-(18). For example here we employ $C_{\text{CFL}} = 100$, to be compared with the inverse of the (absolute value of the) maximum speed $1/|c_{R,\text{max}}| \approx 1/0.0827 \approx 12.1$. This behaviour is likely to be related to the use of the Chebychev grid (clustering at the extrema), the Runge-Kutta scheme, and the fact that the coordinate light speeds in the

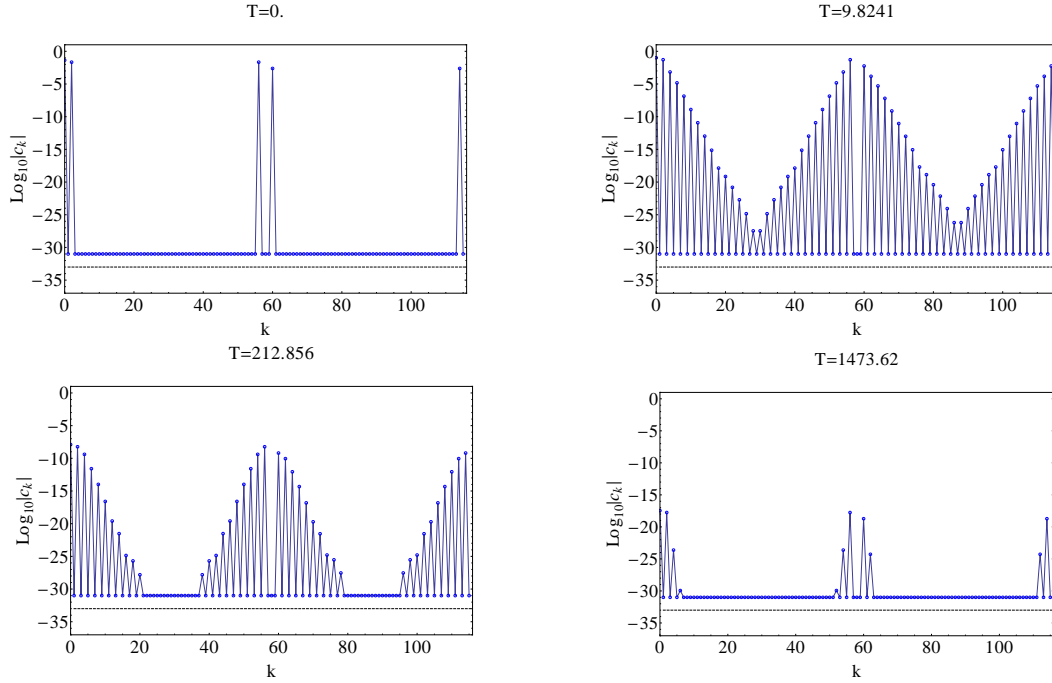


Figure 4. Evolution of the spectral Fourier coefficients of $\Re\{\psi\}$. Given $n_\theta = 29$ angular grid points, the extended (double covering) function is represented by $2n_\theta = 58$ complex Fourier coefficients. The real parts are the first 58, the imaginary parts the second 58. High-frequencies correspond to coefficients in the middle of each part. The left top panel shows that an initially pure multipole can be represented with a few points, but, as a consequence of mode mixing, higher mode coefficients are needed to describe the solution (top right panel). At late times only a few, low-frequency, coefficients are needed because only the lowest multipoles, with slower decay rates, have amplitudes above round-off level (bottom panels).

bulk of the domain are very small, see Fig 2. Note that this is favorable for long-term evolutions and late decay studies. Figures 4 and 5 show the Fourier and Chebyshev expansion coefficients, respectively, of the variable $\Re(\psi)$. The horizontal dashed line at 10^{-33} indicates the nominal round-off level for the quadruple precision employed.

The plot in Fig. 4 refers to a simulation with $n_\theta = 29$ angular points which amounts to $2n_\theta = 58$ complex coefficients for the extended function (double covering.) The coefficients' real parts are the first 58, the imaginary parts the other 58. The coefficients corresponding to highest frequencies are placed in the middle of the real and imaginary sequences. The round-off level is reached in these regions, i.e. $k \sim 36$ and $k \sim 94$. At time $T = 0$ all but five coefficients are zero. This is because the spin-weighted spherical harmonic ${}^{-2}Y_{20} \propto \sin(\theta)^2 = (1 - \cos(2\theta))/2$ and its derivative can be exactly described using the five functions $\{1, \cos(\pm 2\theta), \sin(\pm 2\theta)\}$. During the evolution (e.g. $T \sim 9.8$, top right panel of Fig. 4) all other even-indexed frequency modes are excited, as a consequence of mode mixing. High frequency modes die off faster because they have longer QNM ringing phases and their subsequent power law decays are faster. That is why progressively fewer coefficients are necessary to describe the solution at late times

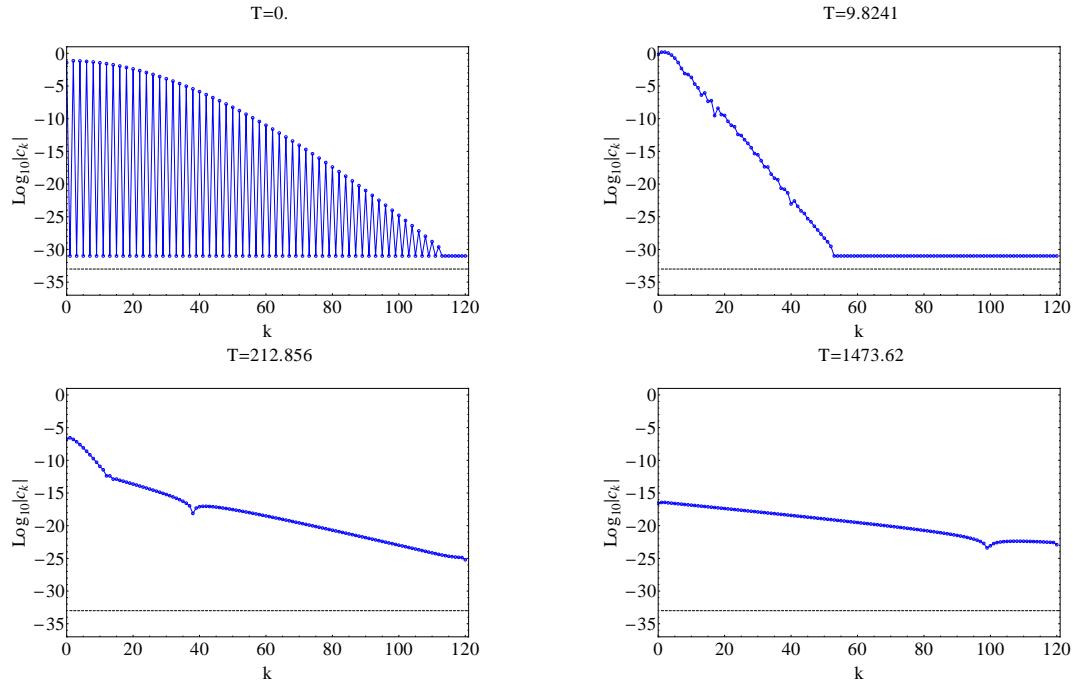


Figure 5. Evolution of the spectral Chebyshev coefficients of $\Re\{\psi\}$ using $n_r = 121$ points. The top left panel illustrates that a narrow initial Gaussian needs already $n_r = 110$ points to be represented at round-off level. The top right panel shows that spectral convergence is achieved and at early times the solution is represented to round-off level. Due to the intrinsic form of the solution at late times, illustrated in Fig. 6, progressively more coefficients are needed to reach round-off in the tail phase (bottom left panel). As long as $|c_0|/|c_{n_r}| \geq 10^6$ (bottom right panel) the solution is not corrupted by high frequency noise.

(see two bottom panels). In the late stages of the simulations only the lowest modes survive and only very few coefficients are required. Note that due to axisymmetry ($m = 0$) only even-indexed coefficients are different from zero in $\Re(\psi)$.

The evolution of the Chebyshev expansion coefficients is shown in Fig. 5. The initial Gaussian with $w = 3000$ requires $n_r \sim 100$ in order to be represented at round-off level. Every second coefficient is vanishing because the Gaussian is set to the center of the domain making it an entirely even function. At early times we observe spectral convergence, but a slower rate of convergence takes progressively over, and more coefficients (large k) are required to describe the function. The use of $n_r \sim 100$ does not allow to reach round-off quadruple precision at late times. This behaviour is due to the intrinsic form of the solution. Because the decay rate at \mathcal{I}^+ is slower than at the horizon, the solution develops large gradients for $R \rightarrow 1$, approaching a step-function-like form at late times. This is clearly described in Fig. 6. Experimentally we observe that until $|c_0|/|c_{n_r}| \geq 10^6$ the simulations are stable, while for $|c_0|/|c_{n_r}| < 10^5$ we observe some high-frequency noise which, eventually, corrupts the simulation and precludes the assessment of the decay rates. In the cases $s < 0$, we found that the use of $n_r \sim 121 \div 141$ points and quadruple precision allows to simulate up to $T \sim 3000 \div 4000$

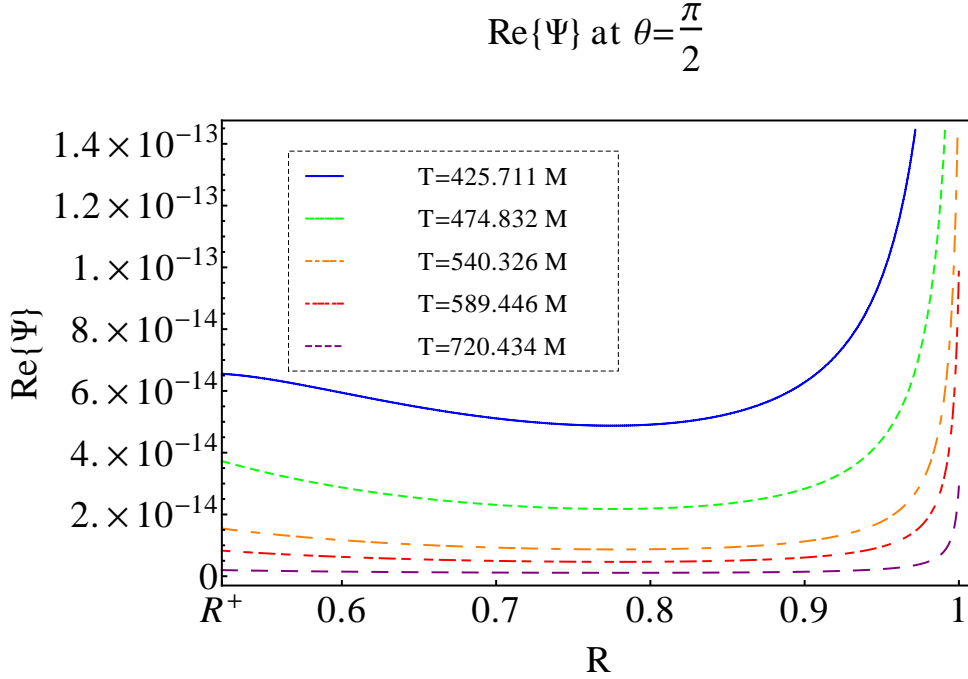


Figure 6. Late time radial profile of the solution. Due to the slower decay rate at \mathcal{I}^+ the solution approaches a step-function like form at late times. This corrupts the spectral convergence of the Chebychev expansion. The figure refers to $s = -2$, $a = 0.9$, $l' = 2$ and ID0 data. The problem is worse for the cases $s > 0$ because the differences between the decay rates at \mathcal{I}^+ and finite radii are larger.

and measure the decay rates with acceptable accuracy (see Sec. 4.2). It may be possible to introduce a modification of the RT coordinates that counters the “piling up” of late tails near the outer boundary to preserve accuracy and convergence for longer times.

For $s > 0$ resolving the radial profile of the late time solution is more challenging. The differences in the decay rates at \mathcal{I}^+ and finite radii are much larger than for $s < 0$ cases, and a large number of spectral coefficients is required. As an example one can consider the decay rates of the overall field of $s = \pm 2$ perturbations with $l' = 2$ and ID1. For $s = -2$ the rates at finite radii and \mathcal{I}^+ are $\mu = 7$ and $\mu = 6$ which differ by only one power. The corresponding rates for $s = +2$ are $\mu = 8$ at the horizon and $\mu = 2$ at \mathcal{I}^+ , which amounts to a difference of six powers and produces large spatial gradients. In these situations about $n_r \sim 400$ points are needed in order to have stability at late times and measure cleanly the tail decays. Because of the quadruple precision, one of such simulations can take up to a month on a modern workstation (the code is serial). However, stable simulations at a more reasonable computational cost can be performed using FD in radial direction. Typical runs are performed with $n_r = 801$ (or $n_r = 1601$), and take about ten hours to reach $T \sim 1500M$, which, in turn, is sufficient to compute the decay rates. Obviously, also in this case, convergence is not completely under control and it is not possible to give a proper error estimate. However, we argue that these results are, at least, *qualitatively* correct because they are compatible with

$$s=-1, a=0.9, l'=1, \text{ID1} - R=1, \theta=\frac{\pi}{2}$$

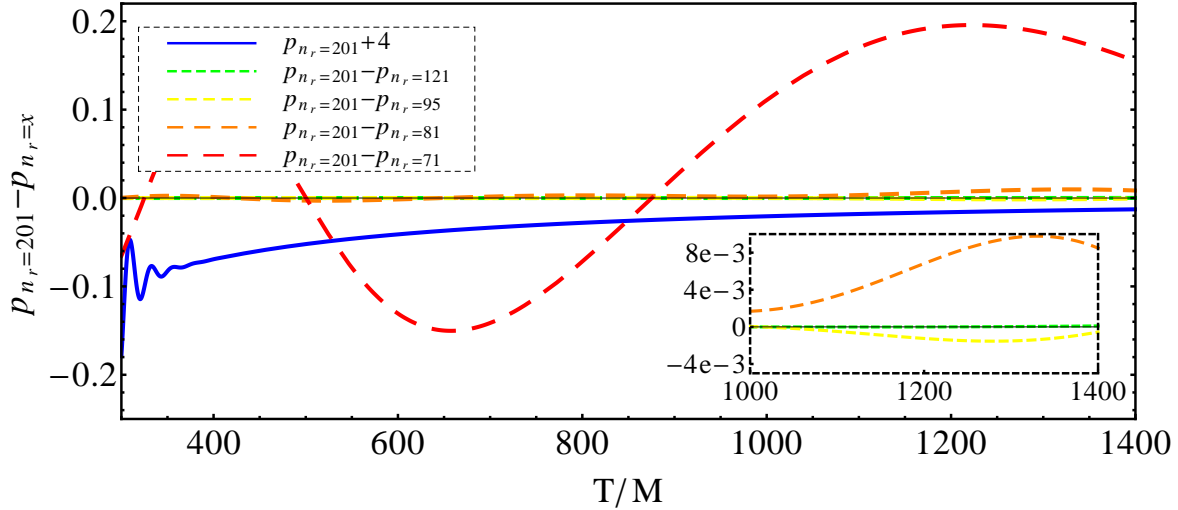


Figure 7. Assessment of LPI accuracy with PS radial differentiation. The solid blue line shows the difference between the LPI of the $l = 1$ projection at \mathcal{S}^+ computed from a $n_r = 201$ simulation and the analytical asymptotic value ($p = -4$). The dashed lines show the differences between the LPIs computed from simulations with different n_r . The plot shows that the deviation from the expected value is less than 0.5% at late times (solid blue line). The self-differences with the target resolution $n_r = 201$ are below 0.05% for $n_r = 121$, of order 0.5% for $n_r = 81$, and of order 5% for $n_r = 71$. The data refer to simulations with $n_\theta = 29$ of a $s = -1$ perturbation with $l' = 1$ and ID1. Extraction is done at $R = 1$ and $\theta = \pi/2$. The runs were done with long-double precision.

those obtained with the PS code. We compared the FD results, for several $s \leq 0$ cases and few $s > 0$ cases, with high resolution PS runs and found very good agreement. As discussed in detail in the next section, the decay rates for $s > 0$ computed with the PS derivative and high resolution typically agree within 0.8% with those computed with the FD derivative. Finally, because all the $s > 0$ results agree with the analytical expectation, we can verify their correctness a posteriori.

4.2. Local-power-index calculation

The power law decay of the field is monitored by the local power index (LPI) [69], calculated as

$$p = \frac{\partial \log |\psi|}{\partial \log T} = T \frac{\Re(\psi) \Re(\partial_T \psi) + \Im(\psi) \Im(\partial_T \psi)}{\Re(\psi)^2 + \Im(\psi)^2}, \quad (24)$$

where the reduction variable $\partial_T \psi$ is employed directly without taking a numerical derivative. Asymptotically in time, the LPI approaches (minus) the decay rate $p \rightarrow -\mu$. The LPIs of the projected modes, p_l , are calculated analogously considering the projections of the fields. For a field of spin s composed of a single azimuthal m -mode,

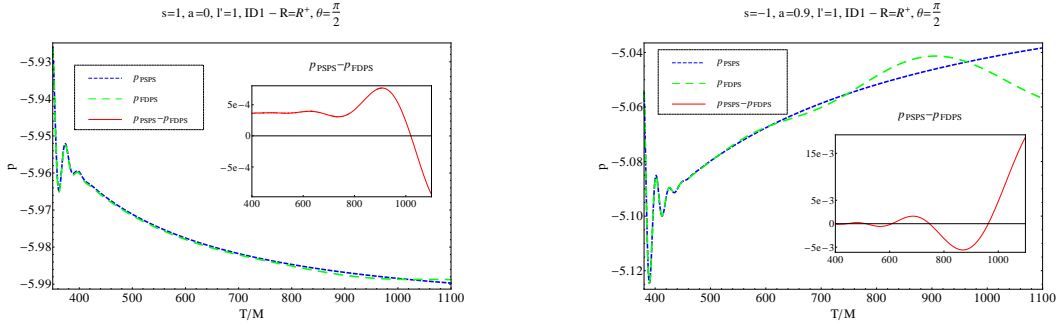


Figure 8. Assessment of LPI accuracy with FD radial differentiation.

The left panel compares the LPIs of the overall field of a $s = +1$ perturbation with $l' = 1$ and ID1 as obtained from simulations with PS radial differentiation with $n_r = 401$ and with FD radial differentiation with $n_r = 801$. Both LPIs are clearly approaching the analytic prediction ($p = -6$) (dashed blue and green lines). The inset shows their difference $\Delta p = p_{\text{PS}} - p_{\text{FD}} \sim 10^{-3}$ at $T = 1000M$. The right panel compares the LPIs of the overall field of a $s = -1$ perturbation with $l' = 1$ and ID1 as obtained from simulations with PS radial differentiation with $n_r = 141$ and with FD radial differentiation with $n_r = 801$. Both LPIs are clearly approaching the analytic prediction ($p = -5$) (dashed blue and green lines). The inset shows their difference $\Delta p = p_{\text{PS}} - p_{\text{FD}} \sim 10^{-2}$ at $T = 1000M$. Both data refer to simulations with $n_\theta = 29$. Extraction is done at $R = R_+$ and $\theta = \pi/2$.

$\psi = \psi_m e^{im\varphi}$, the projections are computed as

$$\psi_{lm}(T, R) = \langle {}^s Y_{lm} | \psi \rangle = \int_0^{2\pi} d\varphi \int_0^\pi d\theta \sin(\theta) \psi_m(T, R, \theta) e^{im\varphi} {}^s Y_{lm}^*(\theta, \varphi). \quad (25)$$

Note that the integration over φ is analytical and reduces to an overall factor 2π . The integration over θ needs to be very accurate to resolve the excited higher modes $l > l'$ which have small amplitudes. Using the Riemann sum or the trapezoidal rule on $(0, \pi)$ is too inaccurate for $n_\theta = 29$ angular points. We performed a spectral integration in the following way. Given a periodic function on $[0, 2\pi]$ and its spectral expansion $f(\theta) \sim \sum_k c_k e^{ik\theta}$, the primitive is approximated by $F(\theta) = \int d\theta f(\theta) \sim \sum_k c_k e^{ik\theta} / (ik)$ and the integral can be computed as $F(\pi) - F(0)$. The primitive function must be computed at the points $\theta = 0, \pi$ which are not included in the numerical grid, so we use interpolation.

The accuracy of this technique was checked by testing the orthonormal relations $\langle {}^s Y_{lm} | {}^s Y_{jm} \rangle = \delta_{lj}$, which yielded the expected *double* precision (employed in the post-processing) for the projections up to $l = 5$ and $n_\theta = 29$.

Finally, we comment on the accuracy of the computed LPIs. Figure 7 illustrates how the accuracy of the LPIs is assessed. The plot refers to the $l = 1$ projected mode of a $s = -1$ perturbation with $l' = 1$ and ID1. PS derivatives are employed in radial direction, and $n_\theta = 29$. The solid blue line shows the difference between the LPI at \mathcal{S}^+ computed from a $n_r = 201$ simulation and the asymptotic value $p = -4$ analytically predicted [46]. The deviation from the expected value is less than 0.5% at late times. This is a general result in all $s \leq 0$ simulations. The dashed lines show the differences

between the LPIs computed from the $n_r = 201$ (target) simulation and others with different n_r . The difference with $n_r = 121$ is below 0.05%, with $n_r = 81$ of order 0.5%, and with $n_r = 71$ of order 5%. Analogously to this case, we find that $n_r \sim 121 \div 141$ points give a reasonably accurate LPI up to $T \sim 1500M$ for most of the simulations.

As discussed in Sec. 4.1 for $s > 0$ perturbations derivatives are computed using FD in the radial direction for efficiency. Specifically, sixth order stencils are employed with no need for artificial dissipation. The CFL factor is $C_{\text{CFL}} = 20$. To assess the accuracy of the LPIs, the outcomes of FD and high-resolution PS simulations are compared for a few test cases. A typical result is shown in Fig. 8, which refers to a $s = \pm 1$ perturbation with $l' = 1$ and ID1. For $s = +1$ (left panel) the PS data are computed with $n_r = 401$ simulations, while the FD data with $n_r = 801$. In both cases the LPIs agree asymptotically with the predicted analytical values ($p = -6$) (dashed blue and green lines) within 0.16% at $T \sim 1100M$. They differ from each other by $\sim 10^{-3}$ ($\sim 0.02\%$), as shown by the solid red line in the inset. Also for $s = -1$ (and in general for $s \leq 0$) the FD differentiation gives accurate results, while not used because for $s \leq 0$ the PS code can be used more efficiently. The right panel of Fig. 8 shows that PS data with $n_r = 141$ differ from FD data with $n_r = 801$ by $\sim 0.4\%$ at $T \sim 1100M$ (see inset). In this case the FD simulation loses accuracy earlier and the green line deviates from the blue line. Still, the LPI is only 1.2% off the predicted asymptotic analytical value ($p = -5$) at $T = 1100M$.

5. Power law tails for axisymmetric perturbations

In this section we report the measured decay rates for $s = 0, \pm 1, \pm 2$ axisymmetric perturbations. In all cases we have considered pure spin weighted spherical harmonics multipole initial data with an axisymmetric profile, i.e. $\psi(\theta) \propto {}^s Y_{l'm'}(\theta)$ with $m' = 0$. The black hole angular momentum is fixed to $a = 0.5$ or $a = 0.9$. The parameters of the function $G(R)$ are $w = 3000$ and $R_0 = 0.8$. For $s \leq 0$ simulations we used PS differentiation in radial direction, while for $s > 0$ FD for the reason discussed in Sec. 4. We used grids of 141×29 and 801×29 points for the spectral and finite difference simulations, respectively. The CFL factor in the PS (FD) simulations is $C_{\text{CFL}} = 100$ ($C_{\text{CFL}} = 20$.) Quadruple (long-double) precision was employed in the $s \leq 0$ ($s > 0$) cases.

The decay rates of the projected modes, μ_l , are given in Tabs. 1, 2 and 3 for $s = 0, \pm 1, \pm 2$ perturbations. The tables refer to the case $a = 0.9$. In the discussion of the decay rates we use the terms up/down-modes as introduced by [56]. Down-modes refer to the below diagonal part of the tables, i.e. $l < l'$, up-modes refer to the upper diagonal and the diagonal part of the tables, i.e. $l \geq l'$. The notation in these tables follows basically the one used by [24] but shall be clarified here. In all cases the asymptotic in time decay rates at the horizon and finite radii are different from those at future null infinity. Thus two μ_l values are reported separated by a vertical line like $x|z$, where x refers to the horizon and finite radii and z to \mathcal{I}^+ . The LPIs at finite radii

$R_+ < R < 1$ vary monotonically between $-x$ and $-z$ at early times and reach the value $-x$ only asymptotically at late times. In practice the x value in the tables is taken close to the horizon. In the cases $s > 0$ and $m = 0$ there are three distinct asymptotic LPIs corresponding to different decay rates at the horizon, finite radii (“finite radii” in these cases means also “excluding the horizon”), and \mathcal{I}^+ . The tables have thus three entries $x|y|z$. The decay rate at finite radii y is taken at a radius $R_+ < \tilde{R} < 1$ where the asymptotic value is reached first. Typically $\tilde{R} \sim 1.05 \div 1.2 R_+$, so it is very close to the horizon, but the exact position is different for each data set. The larger the distance $|R - \tilde{R}|$, the greater the differences between the LPIs $|p(R) - p(\tilde{R})|$ at early times, but, asymptotically in time, $p(R) \rightarrow p(\tilde{R})$ for any finite radius $R_+ < R < 1$. For $R > \tilde{R}$ the LPIs vary monotonically between the values $-y$ and $-z$ (as long as an up-mode does not show splitting). For $R < \tilde{R}$ the transition from y to z depends on the value of s (details are given in the following.)

In some cases there are uncertainties in the assessment of the LPI due to inaccuracies. These can either originate from the loss of convergence in the radial direction due to the unfavorable form of the solution as discussed in Sec. 4.1 or to unresolved higher modes⁺. The symbol \times is employed to indicate that the loss of accuracy at late times prevents an unambiguous determination of the LPI. In cases of LPI splitting we state the decay rate at finite radii in bold phase, **y**, to emphasize that in our relatively short-time simulations we can not confirm its validity for every observer. In particular, the asymptotic decay rate in up-modes with splitting can not always be assessed for observers $R \rightarrow 1$. (In absence of splitting the LPI measurement is position dependent at early times, but in this case there is an unambiguous trend towards the *same* asymptotic decay rate at any finite radii.) In case of exclusion due to symmetries we use the horizontal line $-$ and if we did not simulate that case we use the slash $/$.

5.1. Decay rates for $s = 0$ perturbations

In this section we report the decay rates for the projected modes of $s = 0$ perturbations. The decay rate of the unprojected field is the same as that of the lowest projected mode. For $s = 0$ RT [24] have presented a thorough analysis of decay rates for all four initial data types ID0, ID1, ID2 and ID3 (and also other types). Thus for $s = 0$ we restrict ourselves to measure decay rates for ID0 and ID1 to confirm the correctness of our code.

As shown in Tab. 1 our decay rates are in perfect agreement with the work of [24] and of [25, 61, 56] for ID1. Figure 9 illustrates the LPI calculation for the $l = 0$ and the $l = 2$ projected modes of an $l' = 4$ simulation. From this example one sees that the decay rates of the $l = 0$ projection are clearly identifiable as $\mu_0 = 5|4$ (left panel). Instead, the $l = 2$ LPI lines bend down at radii close to the horizon and assume non-integer values. This is likely due to inaccuracies in higher mode projections so that in these cases we

⁺ Because the decay rate μ_{l^*} of a given projected mode l^* depends on several other modes $l > l^*$ excited by the initial data l' , the accuracy of μ_{l^*} also depends on how well the other modes $l > l^*$ are actually resolved.

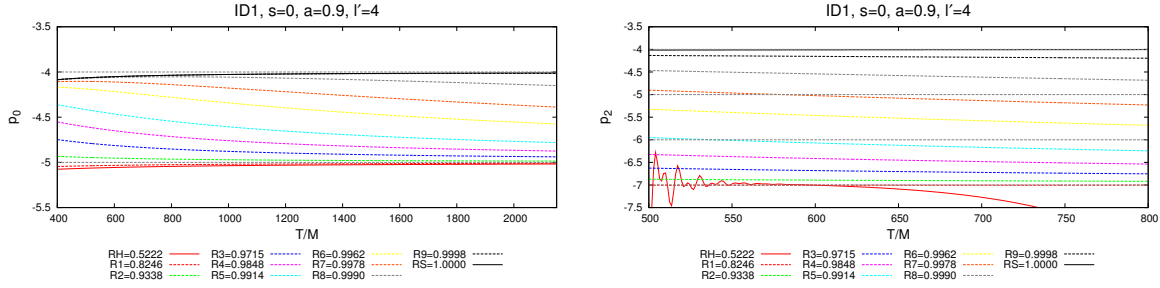


Figure 9. LPIs of the projected modes $l = 0$ (left) and $l = 2$ (right) for a $s = 0$ perturbation with ID1 and $l' = 4$. Different lines refer to different extraction radii. The left panel shows the decay rates approach the values $\mu_0 = 5/4$ at finite radii and \mathcal{I}^+ respectively. Larger radii need longer time to reach their asymptotic decay rate $\mu_0 = 5$. The transition between the decay at R_+ and \mathcal{I}^+ is monotonic. In the right panel there is a clear indication for the asymptotic values $\mu_2 = 7/4$ but the LPIs at close horizon radii depart from being a constant integer. Such cases are marked by brackets in the tables, here as $(7)|4$.

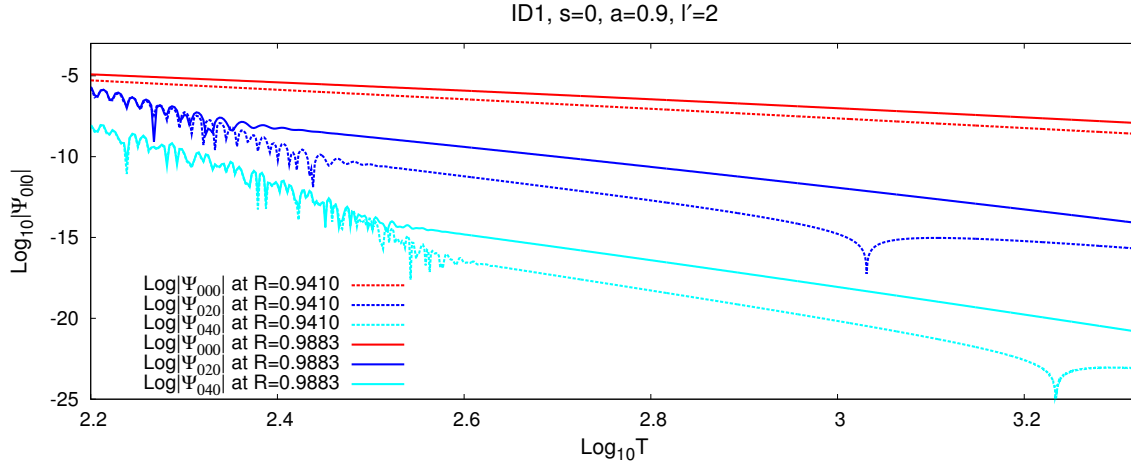


Figure 10. Evolution of the projected modes $l = 0, 2, 4$ of a $s = 0$ perturbation with ID1 and $l' = 2$ at two extraction radii. The dashed lines refer to the modes $l = 0, 2, 4$ at $R = 0.9410$ and the solid lines at $R = 0.9883$. Note that the abscissa is logarithmic. The plot illustrates the difference between far away observers (solid) and observers closer to the horizon (dashed). The observer at $R = 0.9410$ measures a split of p_2 at $T \approx 10^3$ and of p_4 at $T \approx 10^{3.2}$, while the observer at $R = 0.9883$ does not measure the splitting during the simulation time. The corresponding LPIs are reported in Fig. 11.

state the corresponding decay rates in the table with brackets, e.g. $\mu_2 = (7)|4$.

We can unambiguously verify the LPI splitting only for the $l' = 2$ case. Higher values of l' in the initial data seem to produce splitting, but we can not assess unambiguously the values. In agreement with previous results we do not observe splitting for the two lowest initial modes $l' = 0, 1$. The LPI splitting is described by Fig. 10 and Fig. 11, which refer to $l' = 2$ with ID1. The splitting is clearly identifiable by looking at log – log plots. In Fig. 10 the splitting for close horizon observers is visible

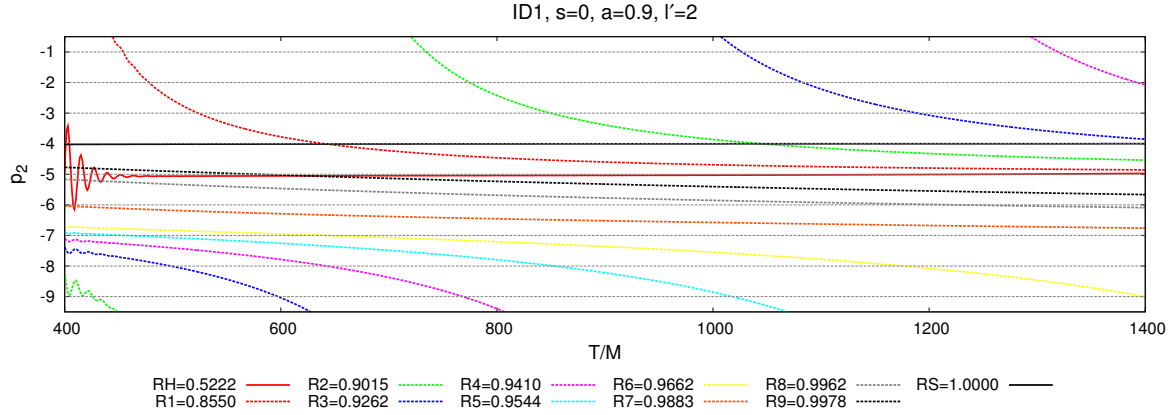


Figure 11. Splitting of the LPIs in the up-mode $l = 2$ for $s = 0$ with ID1 and $l' = 2$ (corresponding to figure 10). The different lines refer to 10 different extraction radii from $R = R_+$ to $R = 1$. The decay rates at the horizon and \mathcal{I}^+ are $\mu_2 = 5/4$. At radii in between the LPI splits, e.g. at $R = 0.9410$ (purple dashed line) the LPI is not a constant integer during the evolution time. Only asymptotically in time the LPI at any finite radius will approach the value $p_2 = -5$. For the observer at $R \sim 0.9883$ (dashed orange line) it is possible to measure an intermediate decay rate $p_2 = -7$. Such cases are marked in bold face in the tables, indicating that at intermediate times different decay rates than the stated ones can be measured by observers far away from the horizon.

as cusps in the tail phases of the $l = 2$ and $l = 4$ modes (dashed blue and cyan lines). Observers far away from the horizon (solid lines) will eventually develop the cusp but at later simulation times. In Fig. 11 the corresponding LPIs are shown for different extraction radii. The asymptotic decay rates at the horizon and \mathcal{I}^+ are, respectively, $\mu_2 = 5$ and $\mu_2 = 4$, as indicated by the solid red and solid black lines. The LPIs at finite radii close to R_+ (dashed lines in the upper part of the plot) approach the value $p_2 = -5$ the faster the closer they are to R_+ . On the contrary, LPIs at finite radii $R > 0.98$ have values $p_2 \simeq -7$ (see the black, grey and orange dashed lines) and are expected to approach the value at R_+ only asymptotically. For these radii the simulated time is not sufficient to observe the splitting towards their asymptotic value. The cusp in the tail of the $l = 2$ mode at $R = 0.9410$ in Fig. 10 corresponds to the dashed purple line in Fig. 11 which bends down at early times and “falls” from the top of the plot at later times. The splitting behaviour basically corresponds to a sign change in the field, which could be probably explained with some analytical argument. Note also that changing the location of the initial Gaussian pulse has a strong effect on the splitting behavior as discussed in [61] (see the latter reference for more insights).

5.2. Decay rates for $|s| = 1$ perturbations

In this section we present our results for $s = \pm 1$ perturbations. Table 2 summarizes the decay rates of the projected modes.

Similarly to the $s = 0$ case, most of the LPIs can be calculated very accurately.

Table 1. Decay rates μ_l for $s = 0$ with ID0 and ID1 at finite radii/future null infinity. Brackets point to uncertainties in the LPI assessment due to possible inaccuracies or not verifiable splitting, \times to ambiguous or immeasurable values, $-$ to modes excluded by symmetry and $/$ to not simulated cases. Bold values denote splitting in time, i.e at intermediate times $p_l \neq -\mu_l$ for $R \lesssim \mathcal{J}^+$.

ID0						
l'	$l = 0$	$l = 1$	$l = 2$	$l = 3$	$l = 4$	$l = 5$
0	3 2	—	5 4	—	7 6	—
1	—	5 3	—	7 5	—	(9) (7)
2	4 3	—	6 4	—	8 6	—
3	—	6 4	—	\times 5	—	\times 7
4	6 5	—	(8) 5	—	\times 6	—
5	/	/	/	/	/	/

ID1						
l'	$l = 0$	$l = 1$	$l = 2$	$l = 3$	$l = 4$	$l = 5$
0	3 2	—	5 4	—	7 6	—
1	—	5 3	—	7 5	—	(9) 7
2	3 2	—	5 4	—	7 6	—
3	—	5 3	—	\times 5	—	\times 7
4	5 4	—	(7) 4	—	\times 6	—
5	—	7 5	—	(9) 5	—	\times 7

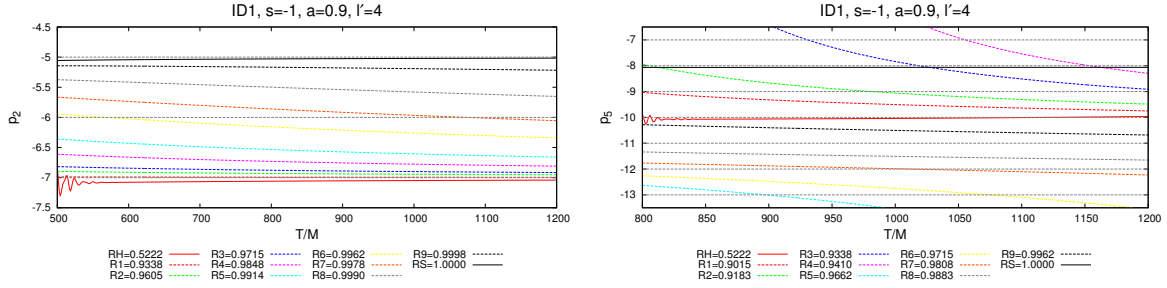


Figure 12. LPIs of the projected modes $l = 2$ (left panel) and $l = 5$ (right panel) of an initial $s = -1$ perturbation with $l' = 4$ and ID1. Different lines refer to different extraction radii. The left panel shows the decay rates $\mu_2 = 7|5$ at finite radii and \mathcal{J}^+ respectively. The transition is monotonic. The right panel shows that LPIs for the $l = 5$ projection split in time. At finite radii including the horizon and \mathcal{J}^+ the decay rates are $\mu_5 = 10|8$, respectively. Only asymptotically in time far out observers like at $R = 0.9962$ (dashed black line) or at $R = 0.9883$ (dashed grey line) will observe the LPI lines bending down and approaching $p_5 = -10$ from above. Such splitting in time is indicated by bold face in the tables.

Looking for example at the left panel of Fig. 12, which refers to the $l = 2$ projection of a $s = -1$ perturbation with ID1 and $l' = 4$, one can see that the decay rates $\mu_2 = 7|5$ can be unambiguously inferred from the plot. Table 2 reveals certain general patterns.

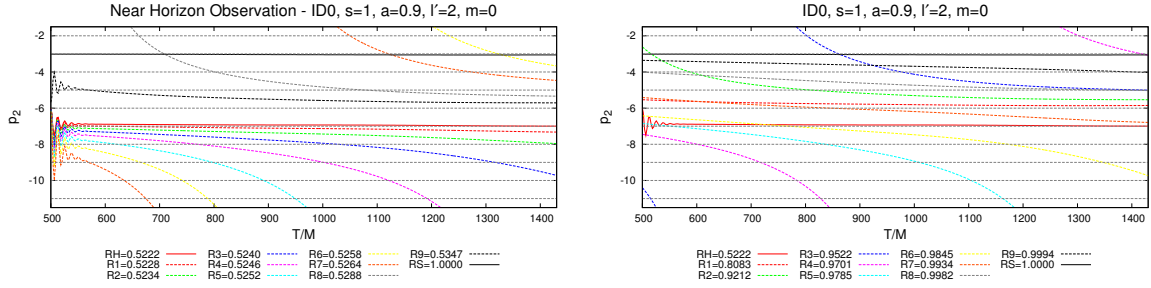


Figure 13. LPIs of the projected mode $l = 2$ of a $s = +1$ perturbation with $l' = 2$ and ID0 measured by observers close to the horizon (left panel) and far away observers (right panel). From both panels one can see the splitting of LPIs into three distinct asymptotic values. The decay rates at R_+ , finite radii excluding R_+ , and \mathcal{I}^+ are $\mu_2 = 7|6|3$. This splitting in space is specific to $s > 0$, $m = 0$ perturbations. The left panel illustrates the behaviour of the LPIs when going from R_+ to $R = 0.5347$. Observers close to R_+ measure initially decay rates close to $p_2 = -7$ but asymptotically they will see the LPI bend down and approach the finite radii rate $p_2 = -6$ from above (in this case observed first at $\tilde{R} \approx 0.6010$). Thus the splitting in space results also in a splitting in time for close horizon observers of $s = +1$, $m = 0$ perturbations. The right panel illustrates the splitting in time for far away observers already shown for $s = 0$ and $s = -1$ perturbations in Fig. 11 and the right panel of Fig. 12.

For example the μ_l at finite radii are always increasing* by one if one steps from one column to the next, i.e. to the higher projected mode. Thus the overall field at finite radii is always dominated by the lowest excitable mode, the $l = 1$ mode for $s = |1|$. This is not true for the decay at \mathcal{I}^+ , where higher projected modes can have the same decay rates as the $l = 1$ mode and can thus dominate the asymptotic signal. Neglecting for a moment the two lowest rows, $l' = 1, 2$, μ_l also increases by one if one steps one row down.

Another interesting result is about the effect of different initial data. Switching from compact to non-compact support ID results in a slower decay. To see this one can compare the tables for ID0 with the tables for ID2 and the tables for ID1 with the tables for ID3. Changing from stationary to non-stationary ID leaves the results for the lowest allowed initial mode l_0 (the first row in the tables) unchanged. However, the second and the third rows seem to be interchanged. From the third row on the difference for finite radii decay rates seems, again, to be just a decrement by one when switching from non-stationary to stationary ID.

There are no other numerical investigations of projected modes' decay rates for $s \neq 0$, $a = 0.9$ including the horizon and \mathcal{I}^+ , but we can compare our results to the theoretical predictions of [46]. In particular, the Green's function calculation provides a result immediately comparable with our ID1 case (see also Appendix B). The decay rates of the overall field as stated in Tab. 1 of [46] can be compared with the first columns of our tables for ID1. Also, though not stated explicitly, the decay rates of projected

* Note that increasing values of μ_l in the tables means actually the LPIs p_l get more negative, i.e. the decay is faster.

modes for ID1 can be read off the effective Green's functions in Eq. (15) (finite radii) and Eqs. (35-36) (\mathcal{I}^+) of [46]. In summary, as shown in the tables, our results for ID1 are in agreement with the predictions by [46] in all tested configurations, except that an apparent difference can be observed for the second lowest allowed initial mode $l' = l_0 + 1$. Comparing with Hod's results, the values in this row are larger by one than the predicted values. However, this discrepancy can be traced back to a missing case distinction in the final parametrization of the result in [46], see Appendix B. With this small correction, there is complete consistency between the analytical and numerical results.

The splitting of LPIs recently reported for $s = 0$ perturbations [24, 25, 61] and verified in Sec. 5.1, is also present in $s \neq 0$ cases. It is convenient to refer to this as a *splitting in time* since intermediate decay rates $p_l \neq -\mu_l$ can be measured at early times while for $T \rightarrow \infty$ a unique asymptotic decay rate μ_l is obtained at any finite radii. An example of splitting in time is reported in the right panel of Fig. 12. The qualitative behaviour is equivalent to the $s = 0$ case previously described, e.g. the far away observer at $R = 0.9962$ (dashed black line) measures at early times an intermediate LPI $p_5 \approx -11$ different from the asymptotic value $\mu_5 = -10$. Only observers at R_+ (solid red line) and close to it (dashed red and green lines) measure the rate $p_5 = -10$ during the simulation time. Such splitting in time is only present in the up-modes: for instance the left panel of Fig. 12 illustrates the LPIs of the down-mode $l = 2$. No splitting is visible and the LPIs vary monotonically between the values $p_2 = -5$ (solid black line) and $p_2 = -7$ (solid red line) at \mathcal{I}^+ and R_+ , respectively.

The splitting in time differs from the splitting in the case of $s > 0$ and $m = 0$ predicted by [46, 49]. In this case the LPI has three distinct asymptotic values at the horizon, at finite radii, and at \mathcal{I}^+ , which could be referred to as a *splitting in space*. The splitting in space is observed in any projected mode as well as in the overall field while the splitting in time is only observed in the up-modes.

The right panel of Figure 13 shows both splittings of LPIs in the projected $l = 2$ mode of a $s = +1$ perturbation with $l' = 2$ and ID0. The decay rates at R_+ and \mathcal{I}^+ are, respectively, $\mu_2 = 7$ and $\mu_2 = 3$, as read off from the solid red and black lines. The splitting in space is clearly visible at the radius $R \approx 0.8083$ which is approaching the value $\mu_2 = 6$ (dashed red line). The left panel of Figure 13 corresponds to the same simulation as the right panel but focuses on observers very close to the horizon. The latter measure at intermediate times LPIs close to the horizon decay rate $p_2 \lesssim -7$ (dashed red and green lines). Instead observers well-off the horizon measure already at early times the LPI $p_2 = -6$. Note that the transition between both takes place in a very small spatial interval because already observers at $R = 0.5288$ measure approximately the asymptotic decay rate $p_2 \approx -\mu_2 = -6$ (dashed grey line).

5.3. Decay rates for $|s| = 2$ perturbations

In this section we present our results for $s = \pm 2$ perturbations.

Table 2. Decay rates μ_l for $s = -1$ (left) at finite radii|null infinity and for $s = +1$ (right) at the horizon|finite radii|null infinity. Brackets point to uncertainties in the LPI assessment due to possible inaccuracies or not verifiable splitting, \times to ambiguous or immeasurable values. Bold values denote splitting in time, i.e. at intermediate times $p_l \neq -\mu_l$ for $R \lesssim 1$.

ID0						ID0					
l'	$l = 1$	$l = 2$	$l = 3$	$l = 4$	$l = 5$	l'	$l = 1$	$l = 2$	$l = 3$	$l = 4$	$l = 5$
1	5 4	6 5	7 6	8 7	9 8	1	6 5 2	7 6 3	8 7 4	9 8 5	\times 9 6
2	5 4	6 5	7 6	8 7	9 8	2	6 5 2	7 6 3	8 7 4	9 8 5	\times \times 6
3	6 5	7 5	8 6	9 7	10 8	3	7 6 3	8 7 3	9 8 4	10 9 5	\times \times 6
4	7 6	8 6	9 6	\times (7)	\times (8)	4	8 7 4	9 8 4	10 9 4	11 (10) 5	\times \times 6
5	8 7	9 7	10 7	(11) 7	\times 8	5	9 8 5	10 9 5	11 10 5	12 11 5	\times \times 6
ID1						ID1					
l'	$l = 1$	$l = 2$	$l = 3$	$l = 4$	$l = 5$	l'	$l = 1$	$l = 2$	$l = 3$	$l = 4$	$l = 5$
1	5 4	6 5	7 6	8 7	9 8	1	6 5 2	7 6 3	8 7 4	9 8 5	\times 9 (6)
2	6 5	7 5	8 6	9 7	10 8	2	7 6 3	8 7 3	9 8 4	10 9 5	\times 10 6
3	5 4	6 5	7 6	8 7	9 8	3	6 5 2	7 6 3	8 7 4	9 8 5	\times \times 6
4	6 5	7 5	8 6	9 7	10 8	4	7 6 3	8 7 3	9 8 4	10 9 5	\times (10) 6
5	7 6	8 6	9 6	10 7	\times 8	5	8 7 4	9 8 4	10 9 4	11 10 5	\times \times 6
ID2						ID2					
l'	$l = 1$	$l = 2$	$l = 3$	$l = 4$	$l = 5$	l'	$l = 1$	$l = 2$	$l = 3$	$l = 4$	$l = 5$
1	4 3	5 4	6 5	7 6	8 7	1	5 4 1	6 5 2	7 6 3	8 7 4	\times 8 5
2	4 3	5 4	6 5	7 6	8 7	2	5 4 1	6 5 2	7 6 3	8 7 4	\times 8 5
3	5 4	6 4	7 5	8 6	9 7	3	6 5 2	7 6 2	8 7 3	9 \times 4	\times \times 5
4	6 5	7 5	8 5	\times 6	\times 7	4	7 6 3	8 7 3	9 8 3	10 \times 4	\times \times 5
5	7 6	8 6	9 6	\times 6	\times 7	5	8 7 4	9 8 4	10 9 4	11 \times 4	\times \times 5
ID3						ID3					
l'	$l = 1$	$l = 2$	$l = 3$	$l = 4$	$l = 5$	l'	$l = 1$	$l = 2$	$l = 3$	$l = 4$	$l = 5$
1	4 3	5 4	6 5	7 6	8 7	1	5 4 1	6 5 2	7 6 3	8 7 4	\times 8 5
2	5 4	6 4	7 5	8 6	9 7	2	6 5 2	7 6 2	8 7 (3)	9 8 (4)	\times 9 (5)
3	4 3	5 4	6 5	7 6	8 7	3	5 4 1	6 5 2	7 6 3	8 7 4	\times \times 5
4	5 4	6 4	7 5	(8) 6	(9) 7	4	6 5 2	7 6 2	8 7 3	9 8 4	\times \times 5
5	6 5	7 5	(8) 5	(9) \times	\times \times	5	7 6 3	8 7 3	9 8 3	10 9 \times	\times \times 5

Qualitatively, $s = -2$ simulations are in complete agreement with $s = 0$ and $s = -1$ simulations. As an example, Fig. 14 shows the LPIs of the $l = 2$ projection for $l' = 4$ and ID0 at different extraction radii. From the plot we can extract the decay rates $\mu_2 = 8|7$, confirming that also for $s = -2$ there are two distinct asymptotic decay rates at any finite radii including the horizon and at future null infinity. The radius dependence is monotonic as already described for the down-modes of $|s| = 0, 1$ perturbations.

The LPI calculations for $|s| = 2$ are summarized in Tab. 3. The decay rates

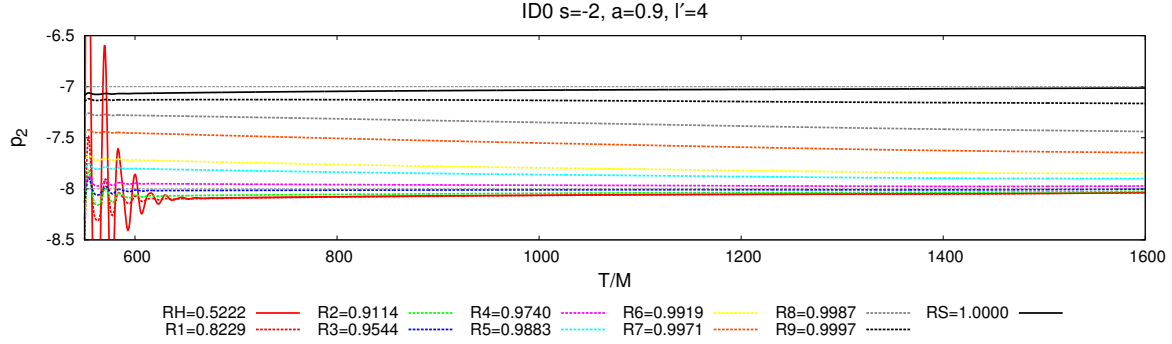


Figure 14. LPIs of the projected mode $l = 2$ of a $s = -2$ perturbation with $l' = 4$ and ID0. Different lines refer to different extraction radii. The asymptotic decay rates extracted from this plot are $\mu_2 = 8|7$ corresponding to the decay rates at finite radii including the horizon and future null infinity. The transition of the LPIs from \mathcal{I}^+ to R_+ is smooth as for $s = 0, -1, +2$ perturbations.

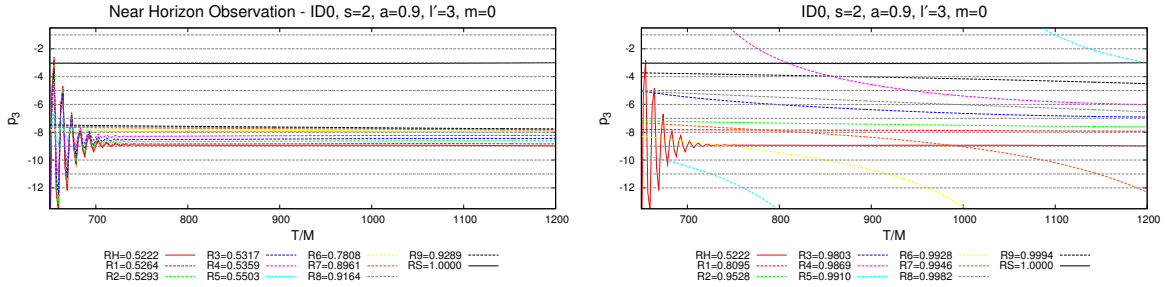


Figure 15. LPIs of the projected mode $l = 3$ of a $s = +2$ perturbation with $l' = 3$ and ID0 measured by close to the horizon observers (left panel) and far away observers (right panel). From both panels one can see the splitting of LPIs into three distinct asymptotic decay rates at R_+ , finite radii excluding R_+ , and \mathcal{I}^+ , here $\mu_3 = 9|8|3$. This splitting in space is special to $s > 0, m = 0$ perturbations. The left panel illustrates the behaviour of the LPIs when going from R_+ to $\tilde{R} \approx 0.5503$. Differently from $s = +1, m = 0$ perturbations (Fig. 13) no splitting in time is observed. The right panel illustrates the splitting in time for far away observers already shown for $s = 0$ and $|s| = 1$ perturbations in Fig. 11 and the right panels of Figs. 12, 13.

follow exactly the same patterns as described in Sec. 5.2 for $|s| = 1$. At finite radii μ_l increases by one when switching to the next higher projection l or the next higher initial mode l' (neglecting again the first two rows $l' = l_0, l_0 + 1$). The overall field is asymptotically dominated by the lowest mode, i.e. for $m = 0$ the $l = 2$ projection. Instead, at \mathcal{I}^+ the $l = 2$ mode is not always the dominant one, because higher modes $l > 2$ can have the same decay rate. Changing from compact to non-compact initial data results in the decay rates decrease by one. Changing from stationary to non-stationary initial data leads to the same modifications of the decay rates as discussed for the case $|s| = 1$. Comparing with the predictions of [46] for ID1 again all our results agree. See again Appendix B for the case $l' = l_0 + 1$.

The splitting in time of the LPIs of up-modes is also observed for $|s| = 2$. As an

example the right panel of Fig. 15 illustrates the splitting in time for the $l = 3$ projection of a $s = +2$ perturbation with $l' = 3$ and ID0. The left panel of Fig. 15 refers to the same simulation as the right panel but concentrates on the LPIs at radii very close to the horizon. The LPIs at R_+ and \mathcal{I}^+ are, respectively, $p_2 = -9$ and $p_2 = -3$, and they are marked by the solid red and black lines. The splitting in space is clearly visible as the LPI is $p_2 = -8$ at the radius $R \approx 0.8095$ (dashed red line in right panel). It is interesting to investigate the close horizon behaviour in the left panel. Differently from the $s = +1, m = 0$ case (compare with Fig. 13, left panel), splitting in time is *not* present for LPIs measured by close horizon observers $R_+ \lesssim R$. This is not a special feature of the particular case shown here. We observe this monotonic transition behaviour in all the projections, as well as the overall field, for all $s = +2, m = 0$ perturbations.

Table 3. Decay rates μ_l for $s = -2$ (left) at finite radii|null infinity and for $s = +2$ (right) at the horizon|finite radii|null infinity. Brackets point to uncertainties in the LPI assessment due to possible inaccuracies or not verifiable splitting, \times to ambiguous or immeasurable values. Bold values denote splitting in time, i.e. at intermediate times $p_l \neq -\mu_l$ for $R \lesssim 1$.

ID0					ID0				
l'	$l = 2$	$l = 3$	$l = 4$	$l = 5$	l'	$l = 2$	$l = 3$	$l = 4$	$l = 5$
2	7 6	8 7	9 8	10 9	2	8 7 2	9 8 3	10 9 4	\times 10 5
3	7 6	8 7	9 8	10 9	3	8 7 2	9 8 3	10 9 4	\times 10 5
4	8 7	9 7	10 8	11 9	4	9 8 3	10 9 3	11 10 4	\times 11 5
5	9 8	10 8	11 8	\times (9)	5	10 9 4	11 10 4	12 11 4	\times \times 5
ID1					ID1				
l'	$l = 2$	$l = 3$	$l = 4$	$l = 5$	l'	$l = 2$	$l = 3$	$l = 4$	$l = 5$
2	7 6	8 7	9 8	10 9	2	8 7 2	9 8 3	10 9 4	\times 10 5
3	8 7	9 7	10 8	11 9	3	9 8 3	10 9 3	11 10 4	\times 11 5
4	7 6	8 7	9 (8)	10 (9)	4	8 7 2	9 8 (3)	10 9 4	\times 10 5
5	8 7	9 7	10 8	11 9	5	9 8 3	10 9 3	11 10 \times	\times \times 5
ID2					ID2				
l'	$l = 2$	$l = 3$	$l = 4$	$l = 5$	l'	$l = 2$	$l = 3$	$l = 4$	$l = 5$
2	6 5	7 6	8 7	9 8	2	7 6 1	8 7 2	9 8 3	\times 9 4
3	6 5	7 6	8 7	9 8	3	7 6 1	8 7 2	9 8 3	\times 9 4
4	7 6	8 6	9 7	10 8	4	8 7 2	9 (8) 2	10 \times 3	\times \times 4
5	8 7	9 7	10 7	\times 8	5	9 8 3	10 9 3	11 (10) (3)	\times \times 4
ID3					ID3				
l'	$l = 2$	$l = 3$	$l = 4$	$l = 5$	l'	$l = 2$	$l = 3$	$l = 4$	$l = 5$
2	6 5	7 6	8 7	9 8	2	7 6 1	8 7 2	9 8 3	\times 9 4
3	7 6	8 6	9 7	10 8	3	8 7 2	9 8 (2)	10 9 (3)	\times 10 \times
4	6 5	7 6	8 7	9 8	4	7 6 1	8 7 (2)	9 8 3	\times \times 4
5	7 6	8 6	9 \times	\times \times	5	8 7 2	9 8 2	10 (9) (3)	\times \times 4

Table 4. Decay rates μ_l for $s = 0$ and $m = 1$ with ID1 at finite radii|null infinity. Brackets point to uncertainties in the LPI assessment due to possible inaccuracies or not verifiable splitting, \times to ambiguous or immeasurable values, $-$ to modes excluded by symmetry. Bold values denote splitting in time, i.e at intermediate times $p_l \neq -\mu_l$ for $R \lesssim 1$. Square brackets point out different values compared to our $m = 0$ tables.

l'	$l = 1$	$l = 2$	$l = 3$	$l = 4$	$l = 5$
1	5 3	—	7 5	—	9 7
2	—	[7] 4	—	[9] 6	—
3	5 3	—	7 5	—	9 7
4	—	(7) 4	—	\times 6	—
5	7 5	—	9 5	—	\times 7

Table 5. Decay rates μ_l for $s = -2$ and $m = 2$ with ID1 at finite radii|null infinity. Bold values denote splitting in time, i.e at intermediate times $p_l \neq -\mu_l$ for $R \lesssim 1$. Square brackets point out different values compared to our $m = 0$ tables.

l'	$l = 2$	$l = 3$	$l = 4$	$l = 5$
2	7 6	8 7	9 8	10 9
3	[7] 6	[8] 7	[9] 8	[10] 9
4	7 6	8 7	9 8	10 9
5	8 7	9 7	10 8	11 9

6. Late time decay of non-axisymmetric perturbations

In this section we report numerical experiments for the late time decay of non-axisymmetric perturbations. We consider $s = 0$ and $s = -2$ perturbations and $a \in [0.9, 1]$. We use again pure multipole ID1, $\psi(\theta) \propto {}^s Y_{l'm'}$, with $m' = 2$ ($m' = 1$) for $s = -2$ ($s = 0$) and $l' = 1, 2, 3, 4, 5$. For $s > 0$ and $a = 0.9$ we discuss the cases $s = +1$, $l' = 2$ and $s = +2$, $l' = 3$, but no further systematic investigations are performed.

6.1. Late time decay for $a = 0.9$

Let us first discuss the case $a = 0.9$. The numerical settings are the same as those for axisymmetric perturbations, but using $R_0 \approx 0.76$. The field dynamics at late times is characterized by power law tails, as in the axisymmetric case.

The decay rates μ_l for $s = 0$ are summarized in Tab. 4. Similarly, the decay rates for $s = -2$ are summarized in Tab. 5. The values different from the axisymmetric case are explicitly indicated by square brackets (compare with Tab. 1, 3.) In the $s = 0$ case the decay of the overall $m = 1$ field can be different from the axisymmetric one, just because the lowest allowed mode for even l' perturbations with $m = 1$ is $l = 2$ instead of $l = 0$. In the $s = -2$ case instead the lowest allowed mode is $l_0 = 2$ for $m = 2$ as well as for $m = 0$. Still the overall $m = 2$ field is found to decay differently from the

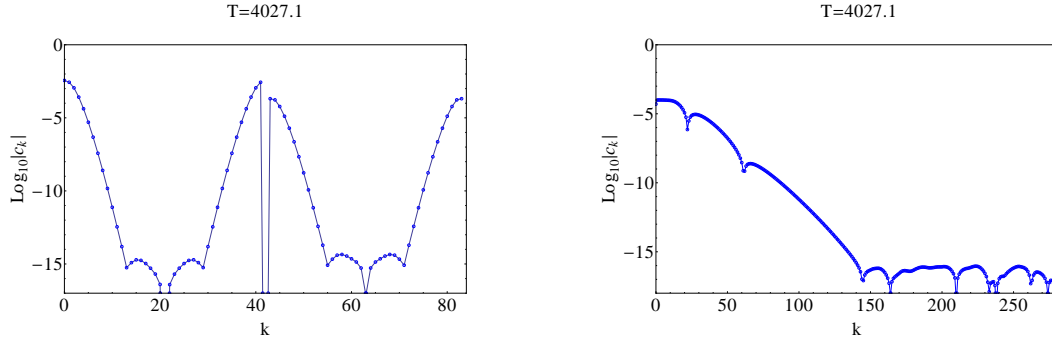


Figure 16. Spectral Fourier (left) and Chebyshev (right) coefficients of the field variable $\Re\{\psi\}$ for $s = -2$ and $a = 0.9999$ at $T \approx 4027M$. The use of $n_\theta = 21$ and $n_r = 281$ points allows to achieve spectral convergence at late times in simulations of perturbations of almost extremal Kerr black holes. Long-double precision is employed here.

axisymmetric analogue for $l' = 3$. As indicated by the tables, the decay rates that differ from the axisymmetric case are only those relative to $l' = 2$ ($l' = 3$) for $s = 0$ ($s = -2$) (second rows in $m \neq 0$ tables). See Appendix B for the mathematical origin of this.

The $s = 0$, $m = 1$ results agree with e.g. [24] and they are consistent with various values reported in the literature [19, 20, 55, 56, 25], where comparable. The $s = -2$ results agree completely with the formulas extracted from the effective Green function computed in [46]. Note that for $m \neq 0$ the parameterization in Eq. (15) and Eqs. (35-36) of [46] yields the correct results also for $l' = l_0 + 1$ (compare Sec. 5).

Furthermore, for $s > 0$ the two simulations with $s = +1$, $l' = 2$ and $s = +2$, $l' = 3$, agree with Hod's formula. For instance, in case of a $s = 2$ and $m = 2$ perturbation we measure $\mu_2 = 7|2$ as opposed to $\mu_2 = 9|8|3$ for $m = 0$, which confirms the prediction that the splitting of LPIs in space is not present for $m \neq 0$.

For what concerns splitting, we confirm that the splitting of LPIs in the $l = 2, 4$ projections of a $s = 0$ and $l' = 2$ perturbation observed for $m = 0$ disappears in the non-axisymmetric case $m = 1$ [24]. By contrast, we observe splitting of LPIs in time in the $l = 3, 5$ projections of a $l' = 3$ perturbation, similarly to the $m = 0$ case.

6.2. Late time decay for $a \rightarrow 1$

In this section we discuss the late time decay behaviour as the angular momentum of the background approaches the extremal value $a = 1$. We consider perturbations with $s = 0$ and $s = -2$ and the Gaussian in the initial data has parameters $R_0 = 0.9$ and $w = 6000$.

Varying the angular momentum a in the range $\{0.9, 0.99, 0.999, 0.9999, 1\}$ in otherwise identical simulations, we observe that the field develops an oscillatory behaviour in space, mostly localized near the horizon and of progressively larger amplitude for $a \rightarrow 1$. The signal extracted at R_+ or \mathcal{I}^+ is characterized by a QNM phase which becomes longer (damping time increases); for $a = 0.9999$ a power law tail

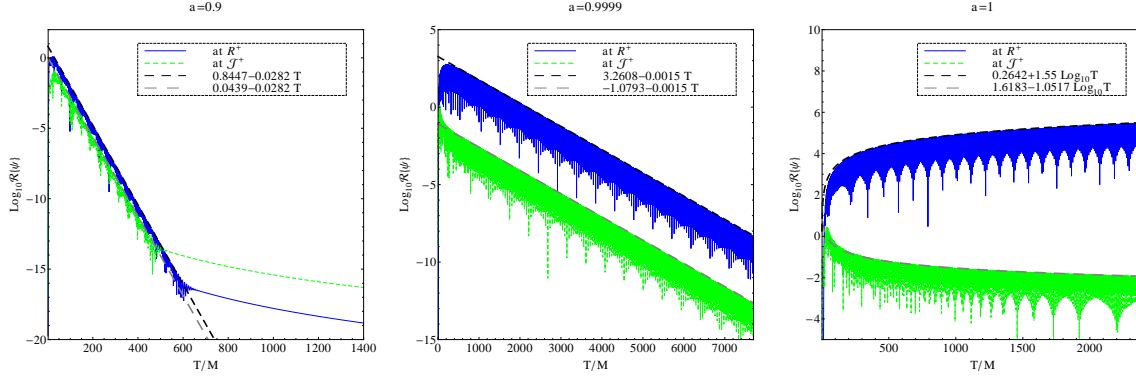


Figure 17. Late time decay of $s = -2$ non-axisymmetric perturbations for highly spinning backgrounds. The plots show the field variable $\Re\{\psi\}$ extracted at $R = R_+$ and $R = 1$ and at $\theta = \pi/2$ for $a \in \{0.9, 0.9999\}$ and $\theta = 1.1345$ for $a = 1$. Initial data are ID1 and $l' = m = 2$. From left to right the field decays with a power law tail ($a = 0.9$), or with an oscillatory behaviour damped by either a slow exponential ($a = 0.9999$) or a power law $1/T$ ($a = 1$).

is not observed up to $T \sim 8000$ but may eventually arise at later times. This behaviour is consistent with the findings of [63, 29], and can be qualitatively understood in terms of modes trapped in the superradiance resonant cavity.

For $a \rightarrow 1$ the amplitude of the oscillating field grows by a few orders of magnitude near R_+ at the beginning of the simulation (especially for $s = -2$). This leads to a step-like function which corrupts convergence if the number of radial grid points n_r is too small (see analogous discussion in Sec. 3). Accurate simulations require PS radial derivatives and $n_r \sim 281$ points for non-extreme cases. For the extreme case we set $n_r = 561$ for $s = 0$ and $n_r = 701$ for $s = -2$. On the other hand the large amplitudes and small damping times allow for the use of long-double instead of quadruple (except for $a = 0.9$ and $s = -2$), which alleviates the computational costs. Due to these facts we observe spectral convergence during the whole simulation time, as shown in Fig. 16 for $s = -2$ and $a = 0.9999$. Both the Fourier coefficients (left panel) and the Chebyshev coefficients (right panel) reach round-off level in approximately straight lines at very late times $T \sim 4000$. Note that the Fourier coefficients contain both even- and odd-indexed frequencies in contrast to the $m = 0$ simulations shown in Fig. 4.

The simulations' outcome is illustrated in Fig. 17 for $s = -2$, $l' = m = 2$, where we report the field extracted at the horizon and \mathcal{I}^+ . On the simulated timescale, the power law tail (left panel) is observed for values $a \leq 0.999$. For larger values ($a = 0.9999$, central panel) an oscillatory and exponentially damped behaviour dominates the dynamics both at the horizon and \mathcal{I}^+ . For $a = 1$ the field remains oscillatory but does not decay exponentially during the simulated time. At the horizon the field amplitude is still growing at $T = 2500$, while at \mathcal{I}^+ the decay departs from an exponential law. A similar qualitative behaviour is observed in the case $s = 0$, $l' = m = 1$.

It is instructive to compare the QNM (complex) frequencies $\omega = (\omega_r, \omega_i)$ extracted

from the $s = -2$ simulations with the data by Berti et al. [11] (listed there up to $a = 0.9999$). The fundamental (longest lived) QNM has the frequency extracted by counting the periods of the signal for long times. (Note that for $a \rightarrow 1$ the frequencies of the overtones accumulate around this value.) Damping times (or ω_i) are extracted by fitting the envelope (maxima) of the field. For $a = 0.9$ we find $\omega \sim (0.6827, 0.0649)$ both at R_+ and \mathcal{I}^+ which agrees very well with the target values $(0.6715, 0.0649)$. For $a = 0.99$ we find $\omega \sim (0.8747, 0.0294)$ compared to $(0.8709, 0.0294)$ and for $a = 0.999$ we get $\omega \sim (0.9584, 0.0105)$ compared to $(0.9558, 0.0105)$. For $a = 0.9999$ we obtain $\omega \sim (0.9862, 0.0035)$, again in agreement with $(0.9857, 0.0035)$. These results also agree with the analytical formulas for QNM frequencies of near-extreme black holes proposed in [70, 71]; the discrepancy is ($\sim 1\%$, $\sim 5\%$) for $a = 0.99$ and ($\sim 0.02\%$, $\sim 0.5\%$) for $a = 0.9999$. The envelope of the field for $a = 0.9999$ is well represented by the fit

$$\log_{10} |\Re\psi| = -1.079(3) - 0.0015064(1)T, \quad (26)$$

where the error on the last significant digit of the coefficients is reported in parentheses. Note that the fitting coefficient proportional to T needs to be divided by $\log_{10}(e)$ to obtain ω_i . In the extreme case we measure $\omega_r \sim 0.9970$ at \mathcal{I}^+ and $\omega_r \sim 1.0015$ at R_+ . It is interesting to notice that this is very close to the superadiance frequency $\omega_+ = m a / (2 M r_+)$ (similarly for $s = 0$ we obtain $\omega_r \sim 0.5011$ both at R_+ and \mathcal{I}^+ in the extreme case). The envelope of the field is best fitted by the power law

$$\log_{10} |\Re\psi| = 1.16(1) - 1.05(2) \log_{10} T, \quad (27)$$

which confirms the expected T^{-1} behaviour for $s = -2$ [29].

7. Conclusion

In this work we have presented a novel approach to time domain numerical solutions of the Teukolsky equation (TE) for generic spin perturbations. The approach is based on the use of the hyperboloidal slicing of the Kerr spacetime, previously introduced by R  acz and T  th (RT) [24], together with a proper rescaling of the field variable that leads to a regular equation for generic spin perturbations (Eq. (12)). The RT coordinates are both horizon penetrating and compactify null infinity (\mathcal{I}^+) at a finite coordinate radius. A generalization is given by Eqs. (8)-(9), which, in particular, allows for a generic compactification. The TE obtained from this 2-parameter family of coordinate transformations and the field rescaling is regular.

Accurate time-domain numerical solutions for generic spin perturbations can be performed employing standard discretization techniques. In particular, long-term, stable 2+1 evolutions are obtained with the method-of-line scheme (e.g. Runge-Kutta time integrators) and either high-order finite differencing or pseudo-spectral spatial derivatives. No boundary conditions are needed, and the computational domain includes the horizon and \mathcal{I}^+ .

As an application, we performed numerical experiments to investigate the late time decays of generic spin perturbations. This problem is a severe test for the robustness of the approach.

In a first series of experiments we investigated power law decays of axisymmetric ($m = 0$) perturbations of spins $s = 0, \pm 1, \pm 2$. A variety of initial data have been used: stationary (ID0, ID2) or non-stationary (ID1, ID3), and compact (ID0, ID1) or non-compact (ID2, ID3) support. In all the cases we used pure multipole initial data. The numerical results for $s = 0$ agree with those reported in the literature. In particular, for non-stationary and compact-support initial data (ID1) the decay rates follow Eq. (1). For what concerns the decay rates of the projected modes of $s \neq 0$ perturbations, it is straightforward to write down *empirical* formulas summarizing our results for $m = 0$. For instance we find for stationary and compact-support initial data (ID0)

$$\mu_l = \begin{cases} l' + l + 3 + \delta, & l' = l_0 \\ l' + l + 2 + \delta, & l' > l_0, \end{cases} \quad (28)$$

at R_+ . Above, $l_0 = \max(|m|, |s|) = |s|$ and $\delta = 0$ in general, but $\delta = 1$ in the special cases $m = 0$ and $s > 0$. The corresponding decay rates at i^+ are given by the same expressions with $\delta = 0$ in all cases. At \mathcal{I}^+ the rates follow

$$\mu_l = \begin{cases} l - s + 2, & l \geq l' \\ l' - s + 1, & l < l'. \end{cases} \quad (29)$$

Similarly for non-stationary, compact-support initial data (ID1) we obtain

$$\mu_l = \begin{cases} l' + l + 3 + \delta, & l' = l_0, l_0 + 1 \\ l' + l + 1 + \delta, & l' > l_0 + 1, \end{cases} \quad (30)$$

at R_+ . The corresponding decay rates at i^+ are given by the same expressions with $\delta = 0$ in all cases, while at \mathcal{I}^+ we get

$$\mu_l = \begin{cases} l - s + 3, & l + 1 \geq l', l' = l_0 + 1 = l + 1 \\ l - s + 2, & l + 1 \geq l', l' \neq l_0 + 1 = l + 1 \\ l' - s, & l + 1 < l' \end{cases} \quad (31)$$

Decay rates for ID2 (ID3) can be easily deduced from those for ID0 (ID1) by decreasing the μ_l by one

$$\text{ID0} \rightarrow \text{ID2}, \text{ID1} \rightarrow \text{ID3} : \mu_l \rightarrow \mu_l - 1. \quad (32)$$

These empirical formulas describe all our numerical results for $s \neq 0$ and $m = 0$.

The decay rates computed for $s \neq 0$ can be compared with Hod's analytic predictions [44, 46]. The comparison is easiest to make for ID1. The results agree with the analytical computation (see Appendix B for a review of the calculation and a small correction for the case $l' = l_0 + 1$ with $m = 0$). For similar type of initial data, Krivan et al [26] reported for $s = -2$ perturbations with the concerned $l' = 3$ initial

mode $\mu = 7.72$. This value was interpreted to asymptotically reach $\mu = 7$ but could be also compatible with our finding of $\mu = 8$. The results of Burko and Khanna for $s = +2$ [51] can not be compared with ours due to the different coordinates used there.

For the first time, to our knowledge, we have verified the LPI splitting (in time) in upper modes of $s \neq 0$ perturbations, as well as the LPI splitting (in space) of $s > 0$, $m = 0$ perturbations. In the latter case, the LPIs reach their asymptotic value first at a radius \tilde{R} close to the horizon. The LPIs measured by $R_+ < R < \tilde{R}$ show a qualitative difference for $s = +1$ and $s = +2$ perturbations: in the former case a splitting in time is observed very close to R_+ .

In a second series of experiments we investigated the late time decay of non-axisymmetric ($m \neq 0$) perturbations, mostly of spins $s = 0, -2$. Focusing on non-stationary and compact support initial data (ID1), we considered the late time behavior of the field for different values of the black hole spin. For $a = 0.9$ we find power law decays which agree with the literature results for $s = 0$ and with [44, 46] for $s = -2$.

If the black hole rotation approaches the extremal limit, the late time decays follow a different law. Perturbations of a rapidly rotating non-extremal background are at very late times still dominated by a weakly damped QNM pattern. In the extremal case, the field decay measured from the simulations is consistent with a T^{-1} power law. These results agree with the findings of [63, 29], the case $s = -2$ is here confirmed for the first time by a numerical time-domain experiment.

In conclusion, the method introduced here is found to be accurate and robust for the solution of the TE in the time domain. To the best of our knowledge these results are the first numerical investigations of the late time decay at future null infinity for $s \neq 0$ perturbations on Kerr. We also view these results as preparatory to the development of an accurate black-hole-binary test-mass laboratory [72, 73, 74, 62, 75]. Some of the results presented may be of interest for the self-force literature.

Acknowledgments

We are indebted to A. Zenginoğlu for discussions and pointing out the rescaling in Eq. (12) for BL coordinates in an early stage of this work. We thank L. Barack and S. Hod for helpful comments on the manuscript. Our work also benefitted from discussions with D. Hilditch and A. Weyhausen. This work was supported in part by DFG grant SFB/Transregio 7 “Gravitational Wave Astronomy”. E.H. wishes to thank the council of Olf and W. Buchholz. S.B. thanks J.D. Bernuzzi for a careful reading of the manuscript.

Appendix A. Equation coefficients and RT metric

The coefficients of Eq. (14) are

$$\begin{aligned}
 C_0 &= \frac{-\frac{1}{2}a^2(R^2-1)^2 - M(R^2-1)R(s+1) + R^2s(s\cot^2(\theta)-1)}{R^3} \\
 C_T &= \frac{1}{R(R+1)(R^2+1)^3} \\
 &\quad \left\{ -a^2(R-1)(R+1)^2(2M(3R^6+5R^4-7R^2-1) - R^4-6R^2-1) \right. \\
 &\quad + 2ia(R+1)(R^2+1)^3 s \cos(\theta) \\
 &\quad - 2[4M^2(R-1)R(R+1)^2(R^4(s+2)+2R^2(s+3)+s) \\
 &\quad + M(R+1)(R^6(7s+3)-2R^5s+13R^4(s+1)-4R^3(s+2)+R^2(5s-7)-2Rs-s-1) \\
 &\quad \left. + 2(R-1)R(R^4s+R^3+2R^2(s+1)+R+s)] \right\} \\
 C_R &= -\frac{(R^2-1)}{2R^2(R^2+1)^3} \\
 &\quad \left\{ a^2(2R^4+5R^2+1)(R^2-1)^2 \right. \\
 &\quad \left. + 2R[M(R^2-1)(R^4(s+3)+2R^2(s+4)+s+1) + 2R(R^4(s+1)+R^2(2s+3)+s)] \right\} \\
 C_\theta &= -\frac{\cot(\theta)}{R} \\
 C_\varphi &= \frac{-aR^2+a-2iRs\cot(\theta)\csc(\theta)}{R^2} \\
 C_{TT} &= \frac{1}{2R(R+1)(R^2+1)^2} \\
 &\quad \left\{ a^2(-(R+1))(32M^2R^6-(64M^2+32M+1)R^4+(32M^2+32M+6)R^2-1) \right. \\
 &\quad + a^2(R+1)(R^2+1)^2\cos(2\theta) \\
 &\quad - 8R[16M^3(R-1)R^2(R+1)^2+8M^2R(R^3-R^2-3R-1) \\
 &\quad \left. + M(R^3-11R^2-5R-1)-R(R+1)] \right\} \\
 C_{RR} &= -\frac{(R^2-1)^2(a^2(R^2-1)^2+4R(M(R^2-1)+R))}{4R(R^2+1)^2} \\
 C_{\theta\theta} &= -\frac{1}{R} \\
 C_{\varphi\varphi} &= -\frac{\csc^2(\theta)}{R} \\
 C_{TR} &= -\frac{2}{(R^2+1)^2} \\
 &\quad \left\{ a^2(R^2-1)^2(2M(R^2-1)-1) + 2(4M^2R(R^2-1)^2+M(3R^2+4R+1)(R-1)^2-2R^2) \right\} \\
 C_{T\varphi} &= \frac{4a(1-2M(R^2-1))}{R^2+1} \\
 C_{R\varphi} &= -\frac{a(R^2-1)^2}{R^3+R}
 \end{aligned}$$

The coefficients of Eq. (15) are given by

$$\begin{aligned}
 \tilde{C}_0 &= C_0 + i m \Re\{C_\varphi\} - m \Im\{C_\varphi\} - m^2 C_{\varphi\varphi} \\
 \tilde{C}_\theta &= C_\theta \\
 \tilde{C}_{\theta\theta} &= C_{\theta\theta} \\
 \tilde{C}_R &= C_R + i m C_{R\varphi} \\
 \tilde{C}_{RR} &= C_{RR} \\
 \tilde{C}_T &= C_T + i m C_{T\varphi} \\
 \tilde{C}_{TR} &= C_{TR} \\
 \tilde{C}_{TT} &= C_{TT}
 \end{aligned}$$

The Kerr metric in RT coordinates can be written

$$ds^2 = (-\alpha^2 + \beta_R \beta^R + \beta_\varphi \beta^\varphi) dT^2 + 2(\beta_R dT dR + \beta_\varphi dT d\varphi) + (\gamma_{RR} dR^2 + \gamma_{\theta\theta} d\theta^2 + \gamma_{\varphi\varphi} d\varphi^2 + 2\gamma_{R\varphi} dR d\varphi), \quad (\text{A.1})$$

where the 3 + 1 metric functions are given by

$$\begin{aligned}
 \beta_R &= \frac{4R(8M^2(R-1)R + 2M(R+1)(\rho^2(R-1)^2 - 1) - \rho^2(R-1))}{\rho^2(R-1)^3(R+1)^2} \\
 \beta_\theta &= 0 \\
 \beta_\varphi &= -\frac{4aMR \sin^2(\theta)}{\rho^2(1-R^2)} \\
 \gamma_{RR} &= -\frac{4(4MR^2 - (4M+1)R-1)(16M^2R^2(R-1) + 4MR(R+1)(\rho^2(R-1)^2 - 1) + \rho^2(R-1)^3)}{\rho^2(R-1)^5(R+1)^3} \\
 \gamma_{\theta\theta} &= \rho^2 \\
 \gamma_{\varphi\varphi} &= \frac{\Sigma^2 \sin^2(\theta)}{\rho^2} \\
 \gamma_{R\varphi} &= -\frac{2a \sin^2(\theta)(16M^2(R-1)R^2 - 4M(R+1)R + \rho^2(R^3 - R^2 + R - 1))}{\rho^2(R-1)^3(R+1)^2} \\
 \alpha &= \left\{ \left(\rho^2(R-1)^2(R^2+1)^2 \left(a^2 \sin^2(\theta) \left(\rho^2 - \frac{4MR}{R^2-1} \right) - \Sigma^2 \right) \right) \right. \\
 &\quad \left[a^2 \sin^2(\theta)(16M^2(R-1)R^2 - 4M(R+1)R + \rho^2(R^3 - R^2 + R - 1)) \right]^2 \\
 &\quad \left. + (R-1)(R+1)\Sigma^2(4MR^2 - (4M+1)R-1) \right. \\
 &\quad \left. (16M^2R^2(R-1) + 4MR(R+1)(\rho^2(R-1)^2 - 1) + \rho^2(R-1)^3) \right]^{-1} \Big\}^{\frac{1}{2}},
 \end{aligned}$$

and the shorthands

$$\begin{aligned}
 r(R) &= \frac{2R}{1-R^2} \\
 \Delta(R) &= r(R)^2 - 2M r(R) + a^2 \\
 \Sigma(R, \theta) &= \sqrt{(r(R)^2 + a^2)^2 - a^2 \Delta(R) \sin^2(\theta)} \\
 \rho(R, \theta) &= \sqrt{r(R)^2 + a^2 \cos^2(\theta)}
 \end{aligned}$$

are used.

Appendix B. Green's function calculation

In this appendix we review the analytical calculation of [45, 44, 46], and specify it for the case of ID1 pointing out explicitly a special case relative to $m = 0$, $s \neq 0$ and pure multipole initial data $l' = l_0 + 1$ that was overlooked in the final parametric formulas of [46]. To avoid confusion we will follow the naming conventions of [46], but keep l' as index of the pure multipole initial data. The calculation is in BL coordinates, and employs the radial tortoise coordinate y defined by $dy = (r^2 + a^2)/\Delta dr$. The main variable Ψ refers to the 2+1 decomposed fields rescaled by $\Delta^{-s/2}(r^2 + a^2)^{-1/2}$ (compare with Eq. (12).)

The solution to the 2+1 TE wave equation for $t > 0$ can be expressed in terms of the retarded Green's function $G(y, \theta, y', \theta', t)$ and the initial data as (see Eq. (6) in [46])

$$\begin{aligned} \Psi(y, \theta, t) = 2\pi \int_0^\pi \int_0^\pi \{ & B_1(y', \theta') [G(y, \theta, y', \theta', t) \Psi_t(y', \theta', 0) + G_t(y, \theta, y', \theta', t) \Psi(y', \theta', 0)] \\ & + B_2(y', \theta') G(y, \theta, y', \theta', t) \Psi(y', \theta', 0) \} \sin \theta' d\theta' dy', \end{aligned} \quad (\text{B.1})$$

where $B_1(y, \theta)$ and $B_2(y, \theta)$ are background dependent complex functions (Eq. (4-5) in [46]), in particular $B_1(y, \theta) = 1 - b_1(y) \sin^2 \theta$.

For non-stationary, pure multipole ID1 $\Psi(y, \theta, 0) = 0$ with $\Psi_t(y, \theta, 0) \propto {}^s Y_{l'm}(\theta)$ only the first of the three terms in Eq. B.1 has to be evaluated,

$$\Psi(y, \theta, t) = 2\pi \int_0^\pi \int_0^\pi B_1(y', \theta') G(y, \theta, y', \theta', t) \Psi_t(y', \theta', 0) \sin \theta' d\theta' dy'. \quad (\text{B.2})$$

The Green's function $G(y, \theta, y', \theta', t)$ can be expressed in terms of its Fourier transform and expanded in the spin weighted spheroidal harmonics ${}^s S_{lm}(\theta, a\omega)$ basis,

$$G(y, \theta, y', \theta', t) = (2\pi)^{-2} \int_{-\infty+ic}^{\infty+ic} \sum_{l=l_0}^{\infty} \tilde{G}_l(y, \theta, y', \theta', \omega) {}^s S_{lm}(\theta, a\omega) {}^s S_{lm}(\theta', a\omega) e^{-i\omega t} d\omega. \quad (\text{B.3})$$

The Green's functions $\tilde{G}_l(y, \theta, y', \theta', \omega)$ admit an analytic solution in terms of two linearly independent solutions of the radial Teukolsky equation, see Eq. (18) of [45]. Given $\tilde{G}_l(y, \theta, y', \theta', \omega)$, to obtain the Green's function it remains to plug it back into Eq. B.3 and evaluate the integral. As discussed in [76] the integration contour is chosen in the lower half of the complex ω plane. The integral consists of three distinct contributions: (i) an integral along the semicircle contributing to the early time solution, (ii) the residues (from the poles of $\tilde{G}_l(y, \theta, y', \theta', \omega)$) in the lower half of the plane, corresponding to the QNM contribution; (iii) an integral along the branch cut $\tilde{G}_l(y, \theta, y', \theta', \omega)$ on the negative imaginary ω axis, contributing to the late time

solution. In the following we consider only the latter and write the Green's function as $G(y, \theta, y', \theta', t) \approx G^C(y, \theta, y', \theta', t)$.

The calculation of the tail contribution to the Green's function, and thus of the solution in Eq. B.1, proceeds by considering a small ω approximation, which corresponds to selecting the large r contribution of the (effective) scattering potential. Considering $\tilde{G}_l(y, \theta, y', \theta', \omega)$ in the small- ω limit the expression for G^C for observers at time like infinity reads (Eq.(12) of [46])

$$G^C(y, \theta, y', \theta', t) = \sum_{l=l_0}^{\infty} K_{ls} (y y')^{l+1} \int_0^{-i\infty} {}^s S_{lm}(\theta, a\omega) {}^s S_{lm}(\theta', a\omega) \omega^{2l+2} e^{-i\omega t} d\omega \quad (\text{B.4})$$

where K_{ls} are constants solely depending on l and s .

Next, appropriate approximations for ${}^s S_{km}(\theta, a\omega)$ have to be introduced. In general, the spheroidal spherical harmonics are defined by the eigenvalue problem

$$L {}^s S_{lm} = (L_0 + L_1) {}^s S_{lm} = -A_{slm} {}^s S_{lm} , \quad (\text{B.5})$$

where L is a differential operator which splits into a ω -independent part with θ -derivatives (L_0) and $L_1 = (a\omega)^2 \cos^2 \theta - 2(a\omega)s \cos \theta$, the ω -dependent part. If $(a\omega)$ is small, one can view L_1 as a perturbation of the operator L_0 and compute a perturbative expansion in $(a\omega)$ [77]. The unperturbed eigenfunctions are the spin weighted spherical harmonics, which are the eigenfunctions in the non-rotating case, i.e. ${}^s S_{lm} = {}^s Y_{lm} + \mathcal{O}(a\omega)$. The expansion then reads

$${}^s S_{lm} = {}^s Y_{lm} + \sum_{i \neq l} \frac{\langle sim | L_1 | slm \rangle}{\Delta A_{li}^{(0)}} {}^s Y_{im} + \dots \quad (\text{B.6})$$

where $\langle sim | F(\theta) | slm \rangle = \int d\Omega {}^s Y_{im}^* {}^s Y_{lm} F(\theta)$, and $\Delta A_{li}^{(0)}$ is the difference between the l -th and i -th unperturbed eigenvalues (independent of θ and ω). The computation of the expansion coefficients requires the evaluation of the integrals $\langle sim | \cos \theta | slm \rangle$ and $\langle sim | \cos^2 \theta | slm \rangle$, the former are non-vanishing for $i = l, l \pm 1$, the latter for $i = l, l \pm 1, l \pm 2$. The expansion in Eq. (B.6) can be written as

$${}^s S_{lm} = \sum_{i=l_0} C_{li} (a\omega)^{|l-i|} {}^s Y_{im} , \quad (\text{B.7})$$

where the coefficients C_{li} depend on $(a\omega)$, but are at leading order independent of $(a\omega)$ for $(a\omega) \ll 1$.

Substituting the unperturbed eigenfunctions in Eq. (B.4), i.e. ${}^s S_{lm} \rightarrow {}^s Y_{lm}$, leads to

$$G^C(y, \theta, y', \theta', t) = \sum_{l=l_0}^{\infty} K_{ls} (y y')^{l+1} {}^s Y_{lm}(\theta) {}^s Y_{lm}^*(\theta') \int_0^{-i\infty} \omega^{2l+2} e^{-i\omega t} d\omega \propto t^{-(2l+3)} , \quad (\text{B.8})$$

which reproduces the Price law with $\mu = 2l + 3$. In order to describe mode coupling and obtain the actual tails on Kerr, one needs to consider the expansion in Eq. (B.6). Renaming some indexes, dropping the s and m indexes, and rearranging some terms, Eq. (B.4) reads

$$G^C = \sum_{l=l_0}^{\infty} \sum_{i=l_0}^{\infty} \sum_{k=l_0}^{\infty} K_{ks} (y y')^{k+1} \int_0^{-i\infty} d\omega e^{-i\omega t} \omega^{2k+2} C_{kl} (a\omega)^{|k-l|} Y_l(\theta) C_{ki} (a\omega)^{|k-i|} Y_i^*(\theta'), \quad (\text{B.9})$$

from which one can read off the l -mode contribution G_l^C defined by $G^C = \sum_l G_l^C$.

We define now an *effective* Green's function for the l -mode that (i) takes into account the non-vanishing terms in the sum over i to the (outer) integral $\int d\theta' \sin \theta' B_1(\theta')^s Y_{l'm}(\theta')$, and (ii) restricts to the lowest powers of $(a\omega)$ that contribute to the sum over k . Step (i) requires the evaluation of the integrals like $\langle sim | \sin^2 \theta' | sl'm \rangle$. In particular, for $m \neq 0$ one has that the non-vanishing terms of $\langle sim | \sin^2 \theta' | sl'm \rangle$ are those given by $i = l', l' \pm 1, l' \pm 2$. For $m = 0$ one has that the non-vanishing terms of $\langle si0 | \sin^2 \theta' | sl'0 \rangle$ are those given by $i = l', l' \pm 2$. The calculation at step (i) gives

$$G_l^{C \text{ eff}} = \sum_{k=l_0}^{\infty} K_{ks} (y y')^{k+1} \int_0^{-i\infty} d\omega e^{-i\omega t} \omega^{2k+2} C_{kl} (a\omega)^{|k-l|} Y_l(\theta) \quad (\text{B.10})$$

$$\{ [1 - b_1(y')] C_{kl'}(a\omega)^{|k-l'|} Y_{l'}^*(\theta') \\ - b_1(y') [C_{kl'-2}(a\omega)^{|k-(l'-2)|} Y_{l'-2}^*(\theta') + C_{kl'-1}(a\omega)^{|k-(l'-1)|} Y_{l'-1}^*(\theta') \\ + C_{kl'+1}(a\omega)^{|k-(l'+1)|} Y_{l'+1}^*(\theta') + C_{kl'+2}(a\omega)^{|k-(l'+2)|} Y_{l'+2}^*(\theta')] \}$$

Note that of the terms in the curly brackets the $C_{kl'\pm 1}$ do not exist for $m = 0$ and the $C_{kl'-2}$ and $C_{kl'-1}$ do not exist, respectively, for $l' = l_0, l_0 + 1$ and $l' = l_0$. Step (ii) requires power counting for given combinations of (l, l') . The freedom of the powers in the curly brackets requires to analyze distinctly the three cases $l' = l_0$, $l' = l_0 + 1$ and $l' \geq l_0 + 2$. In each of these checking the first terms of the k -sum reveals that the lowest power is always obtained by the $k = l_0$ term (however $k > l_0$ terms may amount to the same power). Thus the lowest power of $(a\omega)$ is

$$n_l = \begin{cases} 2l_0 + 2 + |l_0 - l'| + |l_0 - l| & , l' = l_0 , \\ 2l_0 + 2 + |l_0 - (l' - 1)| + |l_0 - l| & , l' = l_0 + 1 , \\ 2l_0 + 2 + |l_0 - (l' - 2)| + |l_0 - l| & , l' > l_0 + 1 . \end{cases} \quad (\text{B.11})$$

The lowest power of $(a\omega)$ for $m = 0$ is instead given by

$$n_l = \begin{cases} 2l_0 + 2 + |l_0 - l'| + |l_0 - l| & , l' = l_0 , \\ 2l_0 + 2 + |l_0 - l'| + |l_0 - l| & , l' = l_0 + 1 , \\ 2l_0 + 2 + |l_0 - (l' - 2)| + |l_0 - l| & , l' > l_0 + 1 , \end{cases} \quad (\text{B.12})$$

as a consequence of the vanishing integrals $\langle si0 | \sin^2 \theta' | sl'0 \rangle$ for $i = l' \pm 1$. It is important to note that for $l' \geq l_0 + 2$, other terms in the sum than the $k = l_0$ can occur with the

power n_l . This is because, while the ω^{2k+2} contribution will always be greater than ω^{2l_0+2} for $k > l_0$, the ω powers that occur with the C coefficients can be smaller for $k > l_0$ than for $k = l_0$.

Finally, the power of the tails for each l -mode can be calculated from the integrals $\int d\omega e^{-i\omega t} \omega^{n_l}$ which give $t^{-\mu_l}$ with $\mu_l = n_l + 1$. The different cases above are actually summarized in the parametric formula in Eq. (15) of [46]. However, the parametrization there seems to miss the special case $l' = l_0 + 1$ and $m = 0$.

The calculation at null infinity is similar to the one above. In this case different approximations for the Fourier transform $\tilde{G}_l(y, \theta, y', \theta', \omega)$ of Eq. (B.3) have to be made but the remaining procedure is unchanged. In particular using again Eq. (B.7) for the approximation of the ${}^sS_{lm}$ and that $\langle sim | \sin^2 \theta' | sl'm \rangle = 0$ unless $i = l', l' \pm 1, l' \pm 2$ one finds the effective Green's function (cf. [46]) of the l -mode

$$G_l^{C \text{ eff}} = \sum_{k=l_0}^{\infty} \tilde{K}_{ks} y'^{k+1} y^{-s} \int_0^{-i\infty} d\omega e^{-i\omega(t-y)} \omega^{k-s+1} C_{kl}(a\omega)^{|k-l|} Y_l(\theta) \quad (\text{B.13})$$

$$\left\{ [1 - b_1(y')] C_{kl'}(a\omega)^{|k-l'|} Y_{l'}^*(\theta') \right.$$

$$- b_1(y') [C_{kl'-2}(a\omega)^{|k-(l'-2)|} Y_{l'-2}^*(\theta') + C_{kl'-1}(a\omega)^{|k-(l'-1)|} Y_{l'-1}^*(\theta')$$

$$+ C_{kl'+1}(a\omega)^{|k-(l'+1)|} Y_{l'+1}^*(\theta') + C_{kl'+2}(a\omega)^{|k-(l'+2)|} Y_{l'+2}^*(\theta')] \left. \right\} ,$$

where \tilde{K}_{ks} is a constant depending on k and s . This Green's function provides again all information to find the decay rates for any pair of (l, l') by going through the sum over k and picking the lowest power of ω . While at i^+ the lowest power is always obtained by the $k = l_0$ term one finds that this is not true at \mathcal{I}^+ . Still in [46] Hod found an appropriate way to parametrize the resulting decay rates but again the parametrization contains an error for $l' = l_0 + 1$ with $m = 0$. In this case the $C_{kl'-1}(a\omega)^{|k-(l'-1)|} Y_{l'-1}^*(\theta')$ term in the curly brackets vanishes so that for $l = l_0$ Hod's prediction is an integer 1 below the actual value. Higher l -modes of the $l' = l_0 + 1, m = 0$ case are predicted correctly because in these cases the $k = l_0 + 1$ term gives the same power of ω without using the $C_{kl'-1}(a\omega)^{|k-(l'-1)|} Y_{l'-1}^*(\theta')$ term of the curly brackets.

References

- [1] S.A. Teukolsky. Rotating black holes - separable wave equations for gravitational and electromagnetic perturbations. *Phys.Rev.Lett.*, 29:1114–1118, 1972.
- [2] Saul A. Teukolsky. Perturbations of a rotating black hole. 1. Fundamental equations for gravitational electromagnetic and neutrino field perturbations. *Astrophys. J.*, 185:635–647, 1973.
- [3] S. Chandrasekhar. *The mathematical theory of black holes*. 1983.
- [4] William H. Press and Saul A. Teukolsky. Perturbations of a Rotating Black Hole. II. Dynamical Stability of the Kerr Metric. *Astrophys. J.*, 185:649–674, 1973.
- [5] J.B. Hartle and D.C. Wilkins. Analytic properties of the teukolsky equation. *Commun. Math. Phys.*, 38:47–63, 1974.
- [6] J.M. Stewart. On the stability of kerr's space-time. *Proc. R. Soc. London, Ser. A*, 344:65–79, 1975.

- [7] B. F. Whiting. Mode stability of the Kerr black hole. *Journal of Mathematical Physics*, 30:1301–1305, June 1989.
- [8] A. Ori. Perturbative Approach to the Inner Structure of a Rotating Black Hole. *General Relativity and Gravitation*, 29:881–929, June 1997.
- [9] Shahar Hod. Late time evolution of realistic rotating collapse and the no hair theorem. *Phys.Rev.*, D58:104022, 1998.
- [10] Leor Barack and Amos Ori. Late time decay of scalar perturbations outside rotating black holes. *Phys.Rev.Lett.*, 82:4388, 1999.
- [11] Emanuele Berti, Vitor Cardoso, and Andrei O. Starinets. Quasinormal modes of black holes and black branes. *Class. Quant. Grav.*, 26:163001, 2009.
- [12] Misao Sasaki and Hideyuki Tagoshi. Analytic black hole perturbation approach to gravitational radiation. *Living Rev.Rel.*, 6:6, 2003.
- [13] Scott A. Hughes. Evolution of circular, nonequatorial orbits of Kerr black holes due to gravitational wave emission. 2. Inspiral trajectories and gravitational wave forms. *Phys.Rev.*, D64:064004, 2001.
- [14] Steve Drasco and Scott A. Hughes. Gravitational wave snapshots of generic extreme mass ratio inspirals. *Phys.Rev.*, D73:024027, 2006.
- [15] Kostas Glampedakis and Daniel Kennefick. Zoom and whirl: Eccentric equatorial orbits around spinning black holes and their evolution under gravitational radiation reaction. *Phys.Rev.*, D66:044002, 2002.
- [16] Kostas Glampedakis, Scott A. Hughes, and Daniel Kennefick. Approximating the inspiral of test bodies into Kerr black holes. *Phys. Rev.*, D66:064005, 2002.
- [17] Sam R. Dolan, Leor Barack, and Barry Wardell. Self force via m -mode regularization and 2+1D evolution: II. Scalar-field implementation on Kerr spacetime. *Phys.Rev.*, D84:084001, 2011.
- [18] Leor Barack. Gravitational self force in extreme mass-ratio inspirals. *Class.Quant.Grav.*, 26:213001, 2009.
- [19] William Krivan, Pablo Laguna, and Philippos Papadopoulos. Dynamics of scalar fields in the background of rotating black holes. *Phys. Rev.*, D54:4728–4734, 1996.
- [20] Mark A. Scheel, Adrienne L. Erickcek, Lior M. Burko, Lawrence E. Kidder, Harald P. Pfeiffer, et al. 3-D simulations of linearized scalar fields in Kerr space-time. *Phys.Rev.*, D69:104006, 2004.
- [21] Luis Lehner, David Neilsen, Oscar Reula, and Manuel Tiglio. The Discrete energy method in numerical relativity: Towards long-term stability. *Class.Quant.Grav.*, 21:5819–5848, 2004.
- [22] Ernst Nils Dorband, Emanuele Berti, Peter Diener, Erik Schnetter, and Manuel Tiglio. A numerical study of the quasinormal mode excitation of Kerr black holes. *Phys. Rev.*, D74:084028, 2006.
- [23] Anil Zenginoğlu and Lawrence E. Kidder. Hyperboloidal evolution of test fields in three spatial dimensions. *Phys. Rev.*, D81:124010, 2010.
- [24] Istvan Rácz and Gabor Zsolt Tóth. Numerical investigation of the late-time Kerr tails. *Class.Quant.Grav.*, 28:195003, 2011.
- [25] Michael Jasiulek. Hyperboloidal slices for the wave equation of Kerr-Schild metrics and numerical applications. *Class.Quant.Grav.*, 29:015008, 2012.
- [26] William Krivan, Pablo Laguna, Philippos Papadopoulos, and Nils Andersson. Dynamics of perturbations of rotating black holes. *Phys. Rev.*, D56:3395–3404, 1997.
- [27] Enrique Pazos-Avalos and Carlos O. Lousto. Numerical integration of the Teukolsky equation in the time domain. *Phys.Rev.*, D72:084022, 2005.
- [28] Dario Nunez, Juan Carlos Degollado, and Carlos Palenzuela. One dimensional description of the gravitational perturbation in a Kerr background. *Phys.Rev.*, D81:064011, 2010.
- [29] Kostas Glampedakis and Nils Andersson. Late time dynamics of rapidly rotating black holes. *Phys.Rev.*, D64:104021, 2001.
- [30] Pranesh A. Sundararajan, Gaurav Khanna, and Scott A. Hughes. Towards adiabatic waveforms

- for inspiral into Kerr black holes: I. A new model of the source for the time domain perturbation equation. *Phys. Rev.*, D76:104005, 2007.
- [31] Pranesh A. Sundararajan, Gaurav Khanna, Scott A. Hughes, and Steve Drasco. Towards adiabatic waveforms for inspiral into Kerr black holes: II. Dynamical sources and generic orbits. *Phys.Rev.*, D78:024022, 2008.
 - [32] Pranesh A. Sundararajan, Gaurav Khanna, and Scott A. Hughes. Binary black hole merger gravitational waves and recoil in the large mass ratio limit. *Phys.Rev.*, D81:104009, 2010.
 - [33] Anil Zenginoğlu and Gaurav Khanna. Null infinity waveforms from extreme-mass-ratio inspirals in Kerr spacetime. *Phys.Rev.*, X1:021017, 2011.
 - [34] Richard H. Price. Nonspherical perturbations of relativistic gravitational collapse. I. Scalar and gravitational perturbations. *Phys. Rev.*, D5:2419–2438, 1972.
 - [35] Tullio Regge and John A. Wheeler. Stability of a Schwarzschild singularity. *Phys. Rev.*, 108:1063–1069, 1957.
 - [36] Frank J. Zerilli. Effective potential for even parity Regge-Wheeler gravitational perturbation equations. *Phys. Rev. Lett.*, 24:737–738, 1970.
 - [37] C. V. Vishveshwara. Scattering of Gravitational Radiation by a Schwarzschild Black-hole. *Nature*, 227:936–938, 1970.
 - [38] William H. Press. Long Wave Trains of Gravitational Waves from a Vibrating Black Hole. *Astrophys.J.*, 170:L105–L108, 1971.
 - [39] M. Davis, R. Ruffini, and J. Tiomno. Pulses of gravitational radiation of a particle falling radially into a schwarzschild black hole. *Phys. Rev.*, D5:2932–2935, 1972.
 - [40] Carlos O. Lousto. A time-domain fourth-order-convergent numerical algorithm to integrate black hole perturbations in the extreme-mass-ratio limit. *Class.Quant.Grav.*, 22:S543–S568, 2005.
 - [41] Sebastiano Bernuzzi, Alessandro Nagar, and Roberto De Pietri. Dynamical excitation of space-time modes of compact objects. *Phys. Rev.*, D77:044042, 2008.
 - [42] Anil Zenginoğlu, Dario Nunez, and Sascha Husa. Gravitational perturbations of Schwarzschild spacetime at null infinity and the hyperboloidal initial value problem. *Class. Quant. Grav.*, 26:035009, 2009.
 - [43] Carsten Gundlach, Richard H. Price, and Jorge Pullin. Late time behavior of stellar collapse and explosions: 1. Linearized perturbations. *Phys.Rev.*, D49:883–889, 1994.
 - [44] Shahar Hod. Mode coupling in rotating gravitational collapse of a scalar field. *Phys.Rev.*, D61:024033, 2000.
 - [45] Shahar Hod. The Radiative tail of realistic gravitational collapse. *Phys.Rev.Lett.*, 84:10–13, 2000.
 - [46] Shahar Hod. Mode coupling in rotating gravitational collapse: Gravitational and electromagnetic perturbations. *Phys.Rev.*, D61:064018, 2000.
 - [47] Leor Barack. Late time dynamics of scalar perturbations outside black holes. 1. A Shell toy model. *Phys.Rev.*, D59:044016, 1999.
 - [48] Leor Barack. Late time dynamics of scalar perturbations outside black holes. 2. Schwarzschild geometry. *Phys.Rev.*, D59:044017, 1999.
 - [49] Leor Barack and Amos Ori. Late time decay of gravitational and electromagnetic perturbations along the event horizon. *Phys.Rev.*, D60:124005, 1999.
 - [50] Leor Barack. Late time decay of scalar, electromagnetic, and gravitational perturbations outside rotating black holes. *Phys.Rev.*, D61:024026, 2000.
 - [51] Lior M. Burko and Gaurav Khanna. Radiative falloff in the background of rotating black hole. *Phys.Rev.*, D67:081502, 2003.
 - [52] Eric Poisson. Radiative falloff of a scalar field in a weakly curved space-time without symmetries. *Phys.Rev.*, D66:044008, 2002.
 - [53] Reinaldo J. Gleiser, Richard H. Price, and Jorge Pullin. Late time tails in the Kerr spacetime. *Class.Quant.Grav.*, 25:072001, 2008.
 - [54] Manuel Tiglio, Lawrence E. Kidder, and Saul A. Teukolsky. High accuracy simulations of Kerr tails: coordinate dependence and higher multipoles. *Class. Quant. Grav.*, 25:105022, 2008.

- [55] Lior M. Burko and Gaurav Khanna. Late-time Kerr tails revisited. *Class.Quant.Grav.*, 26:015014, 2009.
- [56] Lior M. Burko and Gaurav Khanna. Late-time Kerr tails: Generic and non-generic initial data sets, ‘up’ modes, and superposition. *Class.Quant.Grav.*, 28:025012, 2011.
- [57] Anil Zenginoğlu and Manuel Tiglio. Spacelike matching to null infinity. *Phys. Rev.*, D80:024044, 2009.
- [58] Vincent Moncrief. Conformally regular ADM evolution equations, 2000. Talk at Santa Barbara, <http://online.itp.ucsb.edu/online/numrel100/moncrief>.
- [59] Gyula Fodor and Istvan Racz. What does a strongly excited ’t Hooft-Polyakov magnetic monopole do? *Phys. Rev. Lett.*, 92:151801, 2004.
- [60] Gyula Fodor and Istvan Racz. Numerical investigation of highly excited magnetic monopoles in SU(2) Yang-Mills-Higgs theory. *Phys.Rev.*, D77:025019, 2008.
- [61] Anil Zenginoğlu, Gaurav Khanna, and Lior M. Burko. Intermediate behavior of Kerr tails. 2012.
- [62] Sebastiano Bernuzzi, Alessandro Nagar, and Anil Zenginoglu. Binary black hole coalescence in the large-mass-ratio limit: the hyperboloidal layer method and waveforms at null infinity. 2011.
- [63] Nils Andersson and Kostas Glampedakis. A Superradiance resonance cavity outside rapidly rotating black holes. *Phys.Rev.Lett.*, 84:4537–4540, 2000.
- [64] Anil Zenginoğlu. Hyperboloidal foliations and scri-fixing. *Class. Quant. Grav.*, 25:145002, 2008.
- [65] Anil Zenginoğlu. Hyperboloidal layers for hyperbolic equations on unbounded domains. *J.Comput.Phys.*, 230:2286–2302, 2011.
- [66] Mihalis Dafermos and Igor Rodnianski. A Note on boundary value problems for black hole evolutions. 2004.
- [67] Anil Zenginoğlu. A Geometric framework for black hole perturbations. *Phys. Rev.*, D83:127502, 2011.
- [68] Bernd Brügmann. A pseudospectral matrix method for time-dependent tensor fields on a spherical shell. *J. Comp. Phys. (in print)*, 2011.
- [69] Lior M. Burko and Amos Ori. Late time evolution of nonlinear gravitational collapse. *Phys.Rev.*, D56:7820–7832, 1997.
- [70] Shahar Hod. Slow relaxation of rapidly rotating black holes. *Phys.Rev.*, D78:084035, 2008.
- [71] Shahar Hod. Black-hole quasinormal resonances: Wave analysis versus a geometric-optics approximation. *Phys.Rev.*, D80:064004, 2009.
- [72] Alessandro Nagar, Thibault Damour, and Angelo Tartaglia. Binary black hole merger in the extreme mass ratio limit. *Class. Quant. Grav.*, 24:S109–S124, 2007.
- [73] Sebastiano Bernuzzi and Alessandro Nagar. Binary black hole merger in the extreme-mass-ratio limit: a multipolar analysis. *Phys. Rev.*, D81:084056, 2010.
- [74] Sebastiano Bernuzzi, Alessandro Nagar, and Anil Zenginoglu. Binary black hole coalescence in the extreme-mass-ratio limit: testing and improving the effective-one-body multipolar waveform. *Phys.Rev.*, D83:064010, 2011.
- [75] Enrico Barausse, Alessandra Buonanno, Scott A. Hughes, Gaurav Khanna, Stephen O’Sullivan, et al. Modeling multipolar gravitational-wave emission from small mass-ratio mergers. *Phys.Rev.*, D85:024046, 2012.
- [76] Edward W. Leaver. Spectral decomposition of the perturbation response of the Schwarzschild geometry. *Phys.Rev.*, D34:384–408, 1986.
- [77] Leonard I. Schiff. *Quantum Mechanics 3E*. International series in pure and applied physics. McGraw-Hill, 1968.